

Quark excitations through the prism of direct photon plus jet at the LHC

Satyaki Bhattacharya, Sushil Singh Chauhan, Brajesh Chandra Choudhary, and Debajyoti Choudhury

Department of Physics and Astrophysics, University of Delhi, Delhi 110007, India

(Received 25 January 2009; published 20 July 2009)

The quest to know the structure of matter has resulted in various theoretical speculations wherein additional colored fermions are postulated. Arising either as Kaluza-Klein excitations of ordinary quarks, or as excited states in scenarios wherein the quarks themselves are composites, or even in theories with extended gauge symmetry, the presence of such fermions (q^*) can potentially be manifested in $\gamma + \text{jet}$ final states at the LHC. Using unitarized amplitudes and the CMS setup, we demonstrate that in the initial phase of LHC operation (with an integrated luminosity of 200 pb^{-1}) one can discover such states for a mass up to 2.0 TeV. The discovery of a q^* with a mass as large as $\sim 5 \text{ TeV}$ can be achieved for an integrated luminosity of $\sim 140 \text{ fb}^{-1}$. We also comment on the feasibility of mass determination.

DOI: 10.1103/PhysRevD.80.015014

PACS numbers: 12.60.Rc, 13.40.-f, 13.85.Qk

I. INTRODUCTION

The replication of fermion families, while being of profound significance in our understanding of fundamental issues such as CP violation and baryogenesis, nonetheless is puzzling in its own right. Despite its enormous success in explaining all observed phenomena in the regime of particle physics, the standard model (SM) has been entirely unable to proffer any insight into this aspect. Indeed, though the observed mass hierarchies and fermion mixings can easily be accommodated, the SM framework, by its very structure, is unable to even ask such questions of itself. This has led to various speculative ideas seeking to explain these ill-understood issues. Prominent among these are (i) models with extended (family) symmetry, (ii) constructions based on higher-dimensional theory (with or without a string theory motivation), and (iii) the possibility of quark-lepton compositeness, namely, that the SM fermions are not elementary at all.

Many of the ideas discussed in this article would be equally applicable—possibly with minor variations—to theories belonging to any of these three classes. However, for the sake of concreteness, we shall consider theories of compositeness as the basic template for our discussions. Part of the motivation lies in the fact of these theories having a more straightforward ultraviolet completion and, furthermore, suffering from a fewer number of extra channels, thereby reducing possible ambiguities.

In such theories, quarks and/or leptons are no longer the fundamental constituents of matter, but rather are bound states of particles often termed *preons* [1]. The latter are postulated to experience a hitherto unknown force on account of an asymptotically free but confining gauge interaction [2], which becomes very strong at a characteristic scale Λ , thereby leading to the aforementioned composites. In many such models [3,4], though not all, quarks and leptons share at least some common constituents. Such a hypothesis naturally leads to the existence of excited fermion states at a mass scale comparable to the dynamics

of the new binding force. In the simplest models [5], the excited fermions are assumed to have both spin and isospin $1/2$ and to have both their left- and right-handed components in weak isodoublets (i.e. they are vectorlike). Similar is the case for, say higher-dimensional models wherein the known universe is constrained to be on a four-dimensional subspace (a 3-brane) while the SM fields—in particular, the fermions—live in all the dimensions. The analogues of the excited fermions would be the Kaluza-Klein excitations with the mass scale being identified with the inverse of the compactification scale.

As the “excited states” do undergo the SM gauge interactions, they may be produced at colliders operating at high enough energies. On production, they would decay into SM particles, with a particularly favorable channel being the radiative decay into an ordinary fermion and a gauge boson (photon, W , Z , or gluon). At an e^+e^- collider, charged excited fermions could be pair-produced via s -channel (γ and Z) exchanges in collisions, while for excited neutrinos only Z exchange contributes. While t -channel diagrams are indeed possible (W for ν_e^* and γ/Z for e^*), the corresponding contributions to pair production cross sections are generally subdominant on account of the smallness of the coupling [5] between the excited state, its SM counterpart, and a gauge boson. This very coupling, on the other hand, leads to single (as opposed to pair) production of such states (through both s - and t -channel diagrams). This (and other) modes have been used by the four LEP collaborations to essentially rule out such excitations almost up to the kinematically allowed range [6]. Similarly, at HERA, a photon (or equivalently a W/Z) exchange in the t channel could have led to single production of either an excited lepton or an excited quark; corresponding searches have yielded only negative results [7].

If quarks and leptons are not fundamental constituents but only composites, this fact could, in principle, be revealed either through an accumulation of statistics at the Tevatron, or better, by reaching energy scales comparable

to the compositeness scale Λ at the LHC. If Λ is not too high then excited quarks can be produced on shell, while at energies well below Λ , such excitations could manifest themselves through an effective four fermion contact interaction involving SM particles alone [8,9]. The remarkable agreement of CDF and D0 data on dijet, dilepton, and jet + lepton final states with the SM expectations have allowed them to exclude a mass range of 80–720 GeV for excited states [10–12]. On the other hand, a relatively light q^* could be singly produced through qg fusion provided the qq^*g coupling is unsuppressed. With the q^* decaying preferentially into a dijet pair, the signal for such a state can be amplified by an analysis of the angular distributions. This has been studied extensively by both CDF and D0 experiments, leading to new preliminary bounds, namely $\Lambda_+(\Lambda_-) > 2.73(2.64)$ TeV by D0 [13] or $\Lambda > 2.4$ TeV at 95% CL [14] (CDF).

At the LHC, both the ATLAS and the CMS collaborations have predicted the sensitivity in the dijet production mode. The ATLAS collaboration has claimed that the use of dijet angular distributions would allow contact interactions to be probed up to $\Lambda = 10$ TeV with an integrated luminosity of 700 pb^{-1} . The CMS collaboration, on the other hand, has estimated that $\Lambda = 6.2$ TeV can be excluded at 95% confidence level (CL) with a luminosity of 100 pb^{-1} and a 5σ sensitivity could be reached for $\Lambda = 8$ TeV with just 1 fb^{-1} of data [15]. Recently, the possibility of top quark compositeness has been explored through the $pp \rightarrow t\bar{t}\bar{t}$ production process and it has been estimated that a 5σ excess can be observed for a new state of 2 TeV [16].

As an effective tool for the measurement of gluon density inside the colliding hadrons and for a precision test of pQCD predictions, the isolated $\gamma + \text{jet}$ final state has been studied with great detail at the Tevatron collider [17–19] and fixed target experiments [20]. Since the $\gamma + \text{jet}$ final state will be one of the key backgrounds for the $H \rightarrow \gamma\gamma$ search at the LHC, extensive isolation studies addressing all known issues have been performed with this process both theoretically and with detailed detector simulations. It is also an important background for many new physics scenarios e.g. large extra dimensions [21,22], Randall Sundrum gravitons [23], etc. It will, thus, be very interesting to look at $\gamma + \text{jet}$ as a probe of excited quarks in view of the unprecedented energy scale at LHC and the in-depth knowledge of this process gleaned from previous experiments and studies.

The rest of the paper has been organized as follows. In Sec. II we discuss the effective Lagrangian for the theory and new physics contribution. In Secs. III and IV, we, respectively, discuss the backgrounds and event generation. Section V describes the photon and jet algorithms used for the analysis. In Sec. VI we discuss the smearings due to detector resolution effects. Section VII gives the details of kinematical variables used to separate the signal

from the background whereas Sec. VIII deals with isolation study. The significance of signal and discovery are discussed in Secs. IX and X, respectively. In Sec. XI we have presented the result of the analysis. Systematics is discussed in detail in Sec. XII followed by our conclusions and outlook.

II. NEW PHYSICS CONTRIBUTION TO $\gamma + \text{Jet}$ PRODUCTION

In this study, we are interested not in the pair production of any such excited states, but rather in their (additional) contribution to a specific SM final state at a hadronic collider, namely, a hard photon with an associated single jet. Hence, we confine the discussion of the Lagrangian only to the relevant part, namely, the (chromo)magnetic transition between ordinary and excited states. In general, these may be parametrized by

$$\mathcal{L}_{\text{int}} = \frac{1}{2\Lambda} \bar{q}_R^* \sigma^{\mu\nu} \left[\sum_i g_i b_i T_i^a G_{i\mu\nu}^a \right] q_L + \text{H.c.}, \quad (1)$$

where the index i runs over the three SM gauge groups, viz. $SU(3)$, $SU(2)$, and $U(1)$ and g_i , $G_{i\mu\nu}^a$, and T_i^a are the corresponding gauge couplings, field strength tensors, and generators, respectively. Λ denotes the typical scale of these interactions, and the dimensionless constants b_i are, *a priori*, unknown and presumably of order unity.

With these determining both the production rates and the branching into various modes, clearly, the phenomenology would depend considerably on their (relative) sizes. In this article, we shall make the simplifying assumption that the excited states do not couple at all to the weak gauge bosons, but do so with the gluons and the photon. At first glance, this might seem incompatible with an $SU(2) \otimes U(1)$ invariant structure. Note, though, that the coupling with the W^\pm can trivially be omitted by assuming that $b_2 = 0$ in Eq. (1). This, though, would still leave a nonzero coupling with the Z . Similarly, postulating a different relation between b_1 and b_2 could eliminate the coupling with the Z while retaining that to the W^\pm . While complicated embeddings could be the answer to eliminating all couplings with both W and Z , in general this would involve the introduction of more states with masses of the order of or smaller than Λ . Note, though, that either of the choices above (or even any other $|b_2| \lesssim |b_1|$) would not materially influence our analysis. Clearly, the existence of a nonzero b_2 does not affect t -channel contributions. As for the s -channel one, the only influence of b_2 would be through the width of the q^* . However, even for comparable b_i , the width $\Gamma(q^*)$ is clearly dominated by the chromomagnetic moment (b_3) and even the inclusion of a nonzero b_2 would not cause a significant deviation in the branching fraction into $(q + \gamma)$. Thus, the assumption has, at least, the merit of reducing the number of possible couplings and hence simplifying the analysis.

A further point needs to be noted here. With the operators in the effective Lagrangian of Eq. (1) being higher dimensional, the cross sections for any process wherein they play a role would typically grow with the center of mass energy, thus violating unitarity. This is not unexpected in an effective theory. It should be realized that Eq. (1) refers only to the leading terms and the loss of unitarity, to a given order, is presumably cured once even higher-dimensional operators are included. An equivalent way to achieve the same goal is to consider the b_i to be form factors rather than constants. To this end, we shall define the $q^*q\gamma$ and q^*qg vertices to be given by

$$\begin{aligned} \overline{q^*}q\gamma_\mu(p): & \frac{ee_q f_1}{\Lambda} \left(1 + \frac{Q^2}{\Lambda^2}\right)^{-n_1} \sigma_{\mu\nu} p^\nu, \\ \overline{q^*}qg_\mu(p): & \frac{g_s f_3}{\Lambda} \left(1 + \frac{Q^2}{\Lambda^2}\right)^{-n_3} \sigma_{\mu\nu} p^\nu T_\alpha, \end{aligned} \quad (2)$$

where Q denotes the relevant momentum transfer and $f_i \sim 1$ are dimensionless constants proportional to the b_i of Eq. (1). From now on, Eq. (2) defines our theory.¹ For $Q^2 = s$, unitarity is trivially restored as long as the constants $n_i \geq 1$. In the rest of our analysis, we shall confine

$$\begin{aligned} \left. \frac{d\sigma}{d\hat{t}} \right|_{qg \rightarrow q\gamma} &= \frac{-\pi\alpha\alpha_s e_q^2}{3\hat{s}^2} \left[C_{sm} + 2\frac{f_1 f_3}{\Lambda^2} C_I + \frac{f_1^2 f_3^2}{\Lambda^4} C_Q \right], \\ C_{sm} &\equiv \frac{\hat{u}}{\hat{s}} + \frac{\hat{s}}{\hat{u}}, \\ C_I &\equiv \frac{\hat{s}^2(\hat{s} - M_{q^*}^2)\mathcal{F}_s}{(\hat{s} - M_{q^*}^2)^2 + \Gamma^2 M_{q^*}^2} + \frac{\hat{u}^2 \mathcal{F}_u}{\hat{u} - M_{q^*}^2}, \\ C_Q &\equiv (\hat{s}\hat{u} + M_{q^*}^2 \hat{t}) \left[\frac{\hat{s}^2 \mathcal{F}_s^2}{(\hat{s} - M_{q^*}^2)^2 + \Gamma^2 M_{q^*}^2} + \frac{\hat{u}^2 \mathcal{F}_u^2}{(\hat{u} - M_{q^*}^2)^2} \right] + 2M_{q^*}^2 \frac{\hat{s}\hat{t}\hat{u}}{\hat{u} - M_{q^*}^2} \frac{(\hat{s} - M_{q^*}^2)\mathcal{F}_s \mathcal{F}_u}{(\hat{s} - M_{q^*}^2)^2 + \Gamma^2 M_{q^*}^2}, \\ \mathcal{F}_s &\equiv (1 + \hat{s}/\Lambda^2)^{-(n_1+n_3)}, \quad \mathcal{F}_t \equiv (1 - \hat{t}/\Lambda^2)^{-(n_1+n_3)}, \quad \mathcal{F}_u \equiv (1 - \hat{u}/\Lambda^2)^{-(n_1+n_3)} \end{aligned} \quad (4)$$

with the SM result being recovered in the limit $\Lambda \rightarrow \infty$. The new physics contribution to the differential cross section thus depends on four parameters, namely f_1 , f_3 , Λ and the mass of the excited state M_{q^*} .

Whereas these couplings can, in principle, be nondiagonal in flavor, we shall assume that they are not so, thereby evading bounds from possible flavor-changing neutral currents. Further, for the sake of simplicity, we shall also assume these couplings to be generation independent. For Eq. (1) to make sense as an effective Lagrangian, the masses have to be less than Λ (Ref. [24] requires that $M_{q^*} < \Lambda/\sqrt{2}$). Note that as long as we are well below the scale Λ , one of $f_{1,3}$ can always be absorbed in Λ . In our analyses, we would be considering only moderate values for these parameters.

¹While a Lagrangian formulation leading to such vertices would necessitate a seemingly nonlocal Lagrangian, this is not unexpected in an effective theory.

ourselves to a discussion of $n_i = 1$. It should be noted that the collider search limits in the literature actually correspond to $n_i = 0$ (leading to nonunitarized amplitudes and rapidly growing cross sections), and thus, our limits would be more conservative.

With the aforementioned Lagrangian, the width of the q^* is given by

$$\begin{aligned} \Gamma(q^*) &= \Gamma_{q+g} + \Gamma_{q+\gamma}, \quad \Gamma_{q+g} = \frac{2\alpha_s f_3^2}{3} \Gamma_0, \\ \Gamma_{q+\gamma} &= \frac{e_q^2 \alpha f_1^2}{2} \Gamma_0, \quad \Gamma_0 \equiv \frac{M_{q^*}^3}{\Lambda^2} \left(1 - \frac{4m_q^2}{M_{q^*}^2}\right) \left(1 - \frac{m_q^2}{M_{q^*}^2}\right)^2 \end{aligned} \quad (3)$$

and can be very large for a heavy q^* (see Table I). As a fat resonance is often difficult to observe, this will turn out to have profound consequences.

With the introduction of these (flavor-diagonal) vertices as in Eq. (2), the subprocess $qg \rightarrow q\gamma$ acquires a new contribution as portrayed in Fig. 1(a). Adding this contribution to the pure QCD one, the ensuing differential cross section reads

For $q\bar{q} \rightarrow g\gamma$, the Feynman diagrams are as in Figs. 1(c) and 1(d); the differential cross sections are related to those in Eq. (4) by crossing symmetry and are given by

TABLE I. $\Gamma(q^*)$ as a function of $M_{q^*}(= \Lambda)$ for different coupling strengths. Both α_s and α_{em} are evaluated at M_{q^*} .

M_{q^*} (TeV)	Γ (GeV)	
	$f_1 = f_3 = 1.0$	$f_1 = f_3 = 0.5$
0.5	34.4	8.61
1.0	63.6	15.9
2.0	118	29.6
3.0	170	42.6
4.0	221	55.2
5.0	271	67.6
6.0	319	79.8
7.0	367	91.8

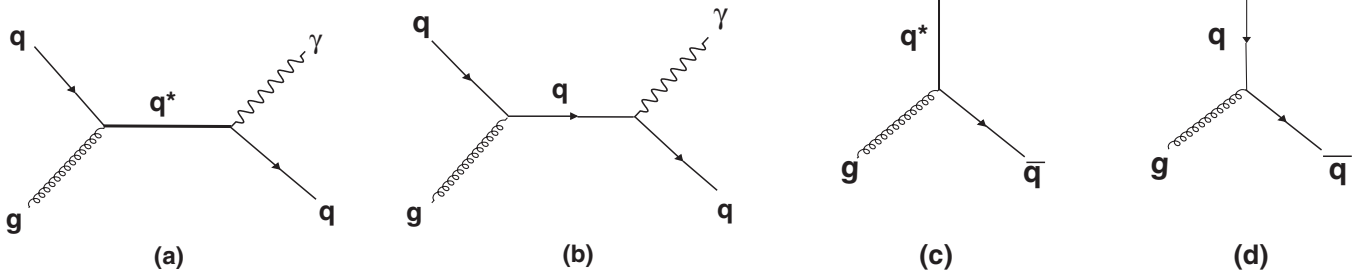


FIG. 1. Production of $\gamma + \text{Jet}$ final state through excited quark mediation (a) and (c) as well as SM processes (b) and (d).

$$\frac{d\sigma}{d\hat{t}} \Big|_{q\bar{q} \rightarrow g\gamma} = \frac{8\pi\alpha\alpha_s e_q^2}{9\hat{s}^2} \left[B_{sm} - 2\frac{f_1 f_3}{\Lambda^2} B_I + \frac{f_1^2 f_3^2}{\Lambda^4} B_Q \right],$$

$$B_{sm} \equiv \frac{\hat{u}}{\hat{t}} + \frac{\hat{t}}{\hat{u}}, \quad B_I \equiv \frac{\hat{t}^2 \mathcal{F}_t}{\hat{t} - M_{q^*}^2} + \frac{\hat{u}^2 \mathcal{F}_u}{\hat{u} - M_{q^*}^2},$$

$$B_Q \equiv \hat{t}\hat{u} \left[\frac{\hat{t}^2 \mathcal{F}_t^2}{(\hat{t} - M_{q^*}^2)^2} + \frac{\hat{u}^2 \mathcal{F}_u^2}{(\hat{u} - M_{q^*}^2)^2} \right] + M_{q^*}^2 \hat{s} \left[\frac{\hat{t} \mathcal{F}_t}{\hat{t} - M_{q^*}^2} + \frac{\hat{u} \mathcal{F}_u}{\hat{u} - M_{q^*}^2} \right]^2. \quad (5)$$

Note that each of the subprocesses described by Eqs. (4) and (5) would revert back to the SM scenario if either of f_1 and f_3 vanish. In Ref. [25], for example, we had considered the case of only a transition magnetic dipole moment (with the chromomagnetic moment f_3 being assumed to be identically vanishing) with the consequence that the simplest way the q^* could manifest itself at the LHC was through a modification of the diphoton production.

Before we end this section, let us note that while Eq. (1) represents the lowest order terms in an effective Lagrangian connecting q^* and q , we could, indeed, have written higher-order (contact) terms such as $(\bar{q}\Gamma_i q)(\bar{q}\Gamma_i q^*)$ or $(\bar{q}\Gamma_i q)(\bar{q}^*\Gamma_i q^*)$, where Γ_i represent combinations of Dirac matrices. Both of these are $\mathcal{O}(\Lambda^{-2})$, and hence we would be justified in neglecting them in an effective theory treatment. The second of these terms would contribute to q^* -pair production. Apart from being kinematically suppressed, this can lead to a contribution to the signal under consideration only if two of the daughter entities from the q^* decays are rendered invisible either by virtue of being outside of the detector acceptance parameters or as a result of merging. The resultant contribution is too small to be of any concern and, in fact, even the much larger QCD contribution to q^* -pair creation resulting from the gauge interaction of the q^* 's is very small for the sensitivity limits that we would turn out to reach. As for the $(\bar{q}\Gamma_i q)(\bar{q}\Gamma_i q^*)$ terms, once again the contribution to $q^* + q/g$ production is only $\mathcal{O}(\Lambda^{-4})$ and hence much smaller than the leading terms of Eqs. (4) and (5). Additionally, the need to lose a jet

further suppresses the rates. And while such terms would also contribute to $\Gamma(q^*)$, the corresponding partial width would be suppressed by a factor $\sim M_{q^*}^2/(4\pi\Lambda^2)$ or smaller compared to those of Eq. (3).

III. BACKGROUNDS

The $\gamma + \text{jet}$ final state can be mimicked by many known processes of the SM. We consider all the leading contributions (both the physics backgrounds as well as the detector ones) and broadly categorize these into three classes viz.,

- (i) Type I: where a photon and a hard jet is produced in the hard scattering.
- (ii) Type II: QCD dijet, where one of the jets fragments into a high E_T π^0 which then decays into a pair of overlapping photons and, hence, is registered as a single photon. Moreover, in some cases the electromagnetic fraction of a jet can mimic a photon in the detector.
- (iii) Type III: Photon + dijet production, where one of the jets is either lost or mismeasured. This could proceed either from hard processes such as $q\bar{q} \rightarrow q\bar{q}\gamma$, $gg\gamma$ (with all possible interchanges of initial and final state partons) or result from $W/Z + \gamma$ production with the heavy bosons decaying into a pair of jets.

While the leading contributions to the Type I background emanates from the SM amplitudes of Fig. 1, a further contribution is displayed in Fig. 2. In Figs. 3 and 4, we show the major contributing Feynman diagrams for the Types II & III backgrounds, respectively.

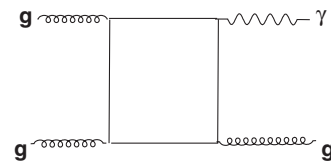
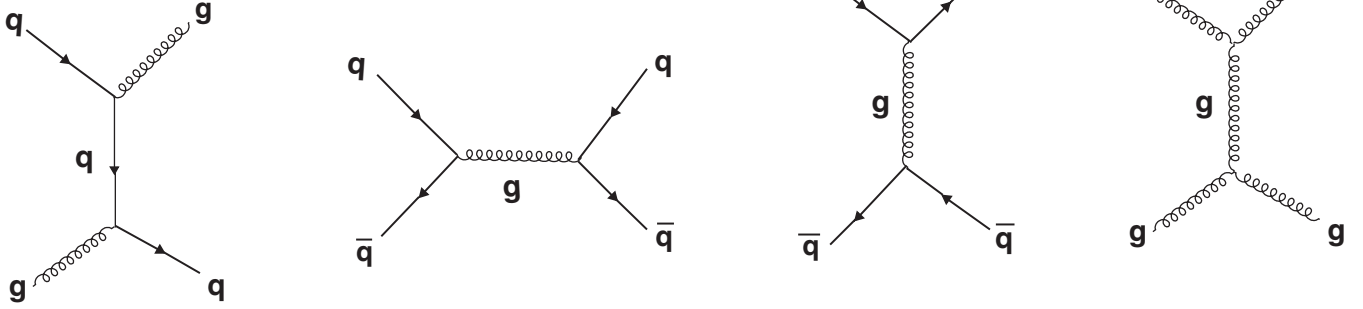
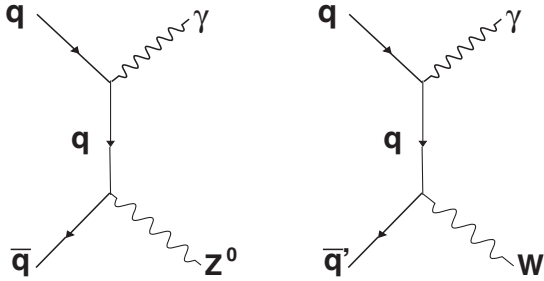


FIG. 2. Type I background: Additional contribution from gluon fusion. Lowest order background emanates from (b) and (d) in Fig. 1.


 FIG. 3. Type II background: QCD jet production where a jet fakes a photon giving a $\gamma + \text{Jet}$ final state.

 FIG. 4. Type III background: Here W/Z^0 decays to two jets and only one of the jets passes the trigger threshold.

In Table II we show the production cross section for all backgrounds in different \hat{P}_T ranges.

At the LHC, the Type I background is dominated by the Compton process ($qg \rightarrow \gamma q$), while the other two subprocesses, namely, annihilation ($q\bar{q} \rightarrow \gamma g$) and gluon fusion ($gg \rightarrow \gamma g$) contribute only a small fraction for relatively small transverse momenta (e.g., for $P_T^{\gamma, \text{jet}} \lesssim 1$ TeV). For larger P_T s, the annihilation subprocess can contribute up to about $\sim 24\%$ of the total Type I background.

The Type II background accrues mainly from $qg \rightarrow qg$, $q\bar{q} \rightarrow q\bar{q}$, and $gg \rightarrow gg$. For $\hat{P}_T \geq 180$ GeV, the total dijet production cross section is $\sim 10^4$ times larger than the Type I background. However, with the probability of a jet faking a photon in the detector being only $\sim 10^{-3}-10^{-4}$, the Type

II background reduces to the same order as the Type I. Moreover, with increasing transverse momenta the QCD dijet falls very rapidly ($\sim P_T^{-4}$), thereby suggesting a simple mechanism of suppressing this background.

Although the total Type III background is very small compared to the Compton and annihilation processes of Type I, for the P_T range under consideration in this analysis, it turns out to be of the same order as $gg \rightarrow \gamma g$. And while nonresonant subprocesses (such as the $\mathcal{O}(\alpha_s^2 \alpha)$ contributions to $q\bar{q} \rightarrow q\bar{q}\gamma$ or $gg \rightarrow q\bar{q}\gamma$) can, in principle, be substantial, note that these, in some sense are related to the much larger Type I and Type II backgrounds. Consequently, the former are typically suppressed when appropriate phase space cuts are imposed to reduce the latter.

IV. EVENT GENERATION AND CUTS

The event generation for signal and different background processes was done with PYTHIA-v6.325 [26]. For signal event generation the matrix elements of Eqs. (4) and (5) were implemented inside the PYTHIA framework. We used the following common parameters and PYTHIA switches:

- (i) Parton distribution function(PDFs): CTEQ 5L [27];
- (ii) $Q^2 = \hat{s}$;
- (iii) Multiparton interaction(MPI): ‘‘ON’’;

 TABLE II. Production cross section in different \hat{P}_T bins for various standard model backgrounds with $\gamma + \text{Jet}$ final state.

Subprocess	50–100 GeV (pb)	100–200 GeV (pb)	200–400 GeV (pb)	400–600 GeV (pb)	600–1000 GeV (pb)	1000–1500 GeV (pb)	1500 GeV and above (pb)
$qg \rightarrow \gamma q$	7.22×10^3	569	36.3	1.53	2.22×10^{-1}	1.19×10^{-2}	7.6×10^{-4}
$q\bar{q} \rightarrow \gamma g$	652	65.3	5.56	3.18×10^{-1}	5.67×10^{-2}	3.76×10^{-3}	2.8×10^{-4}
$gg \rightarrow \gamma g$	1.79	8.6×10^{-2}	3.1×10^{-3}	7.04×10^{-5}	6.32×10^{-6}	1.75×10^{-7}	5.8×10^{-9}
QCD Jet	1.71×10^7	9.70×10^5	4.44×10^4	1.39×10^3	171	8.19	5.34×10^{-1}
$^a Z(jj) + \gamma$	5.08	8.49×10^{-1}	9.50×10^{-2}	6.23×10^{-3}	1.16×10^{-3}	8.48×10^{-5}	6.46×10^{-6}
$^a W(jj) + \gamma$	4.80	6.93×10^{-1}	6.19×10^{-2}	4.16×10^{-3}	7.39×10^{-4}	4.67×10^{-5}	2.99×10^{-6}

^aHere the branching fraction is taken into account.

- (iv) Initial state radiation (ISR) and final state radiation (FSR): “ON.”

To get enough statistics for both the signal and the backgrounds, we divided the whole analysis into three phase space regions (in a relative sense) determined by the value of the P_T of the final state γ and the jet. For this purpose, the following \hat{P}_T (CKIN(3) parameter of PYTHIA) criteria were used for different mass points of signal:

- (i) $\hat{P}_T \geq 180$ GeV(low): 1.0–3.0 TeV,
- (ii) $\hat{P}_T \geq 450$ GeV(medium): 3.5–4.5 TeV,
- (iii) $\hat{P}_T \geq 950$ GeV(high): 5.0–6.0 TeV.

A total of 16 mass points, 11 for coupling strength $f_1 = f_3 = 1.0$ (with a step size of 0.5 TeV) and 5 for $f_1 = f_3 = 0.5$ were generated. The different backgrounds were also generated in various \hat{P}_T range. No pseudorapidity restriction was applied while generating the events as the large \hat{P}_T cut requirement naturally restricts the events to well within $|\eta| < 5.0$. We must also mention here that in the final selection of γ , we have used the fiducial volume of the electromagnetic calorimeter of the CMS detector i.e. $|\eta| \leq 2.5$ with $1.444 \leq |\eta| \leq 1.566$ excluded on account of the insensitive region between the barrel and the endcaps [28]. The jets were selected up to $|\eta| \leq 3.0$ only, because of poor resolution in the forward calorimeter.

Figure 5 displays the deviation in the total cross section of $qg \rightarrow \gamma + \text{jet}$ from its SM value as a function of $M_{q^*} (= \Lambda)$. That the functional deviation is approximately a Λ^{-2} one attests to the fact that, for large Λ , the new physics contribution is dominated by the interference term in Eqs. (4) and (5) rather than the pure Λ^{-4} term. On the other hand, had we imposed harder cuts on the photons, the latter term would have dominated. However, since this would have led to a much-reduced event rate (and, thereby the sensitivity), we desist from doing so. For $\Lambda \geq 6$ TeV, this excess becomes almost negligible.

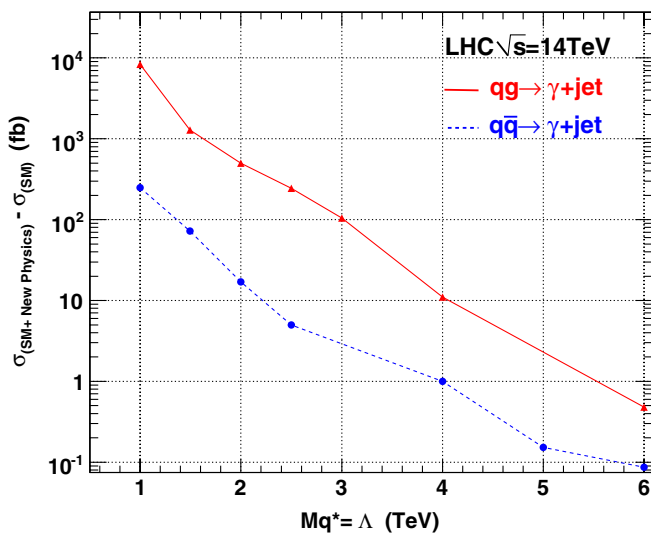


FIG. 5 (color online). Deviation of the total cross section from the SM value as a function of $M_{q^*} (= \Lambda)$ for $\sqrt{s} = 14$ TeV.

V. PHOTON AND JET CANDIDATES AT THE GENERATOR LEVEL

Although a mass peak in the signal will appear as an excess of events over the continuum SM background, the significance for such an observation will depend on the size of this continuum. Hence, to enhance the signal peak, it is necessary to reduce the backgrounds as much as possible. For the signal under investigation, QCD dijet production comprises the largest background, as it mimics the $\gamma + \text{jet}$ final state when one of the jet fakes a photon. To estimate this background reasonably at the generator level, it is a must to have a proper understanding of the reconstruction algorithm for a specific design of the detector rather than limit ourselves to only a partonic level study of a photon and jet(s) final state.

To this end, we use a clustering algorithm to account for fake photons arising from jets [29]. While a detailed discussion of the photon reconstruction algorithm at the generator level can be found in a previous work [25], we present here, for the sake of completeness, a brief recapture of the same. The electromagnetic calorimeter (ECAL) of the CMS detector consists of $PbWO_4$ crystals, with each covering 0.0175×0.0175 (equivalently, 1°) in the $\Delta\eta - \Delta\phi$ space (ϕ being the azimuthal angle). Using the “hybrid” algorithm [30], we choose a seed for the clustering such that it has a minimum P_T of 5 GeV. We consider only those final state electromagnetic particles (i.e., γ, e^\pm) such that each of the distances $\Delta\eta$ and $\Delta\phi$ from the seed object is less than 0.09 (corresponding to a 10×10 crystal size for the CMS detector). A photon candidate is either a direct photon or other electromagnetic objects such as $\pi^0, \eta, \rho^0, \omega$, etc. The main contributor to fake photons are $\pi^0 \rightarrow \gamma\gamma$ (~81%) and $\eta \rightarrow \gamma\gamma$ (~12%) with other sources contributing subdominantly.

For jet reconstruction, various algorithms have been used by different collider experiments. These include the MidpointCone [31], IterativeCone [32,33], and the K_t algorithms [34–36]. The K_t and MidPoint algorithms are used mostly for offline analysis. Since we have used the CMS setup in our analysis, we use the IterativeCone algorithm to reconstruct jets at the generator level. Being much faster, this is commonly used for software based triggers. While the first algorithms for the jets at the hadron colliders started with simple cones in the $\Delta\eta - \Delta\phi$ space [37], clustering techniques have greatly improved in sophistication over the last two decades [31,34].

For a real detector, the first step in the reconstruction, before invoking the jet algorithm, is to apply noise and pile-up suppression with a set of cuts on E_T . To make “perfect detector jets,” we use a seed P_T cut on the P_T -ordered final state particles and select only those which have a transverse momentum above the

required minimum² of $P_{T \text{ seed}} \geq 1.0$ GeV. Once the seed is selected, we search around for all the particles in a cone of $\Delta R \leq 0.5$. The objects inside the cone are used to calculate a *proto-jet* direction and energy using the E-scheme ($\sum P_i$). The computed direction is then used to seed a new proto-jet. The procedure is repeated until both the energy and the direction of the putative jet is stable between iterations. We quantify this by requiring that the energy should change by less than 1% and the direction by less than $\Delta R = 0.01$. When a stable proto-jet is found, all objects in the proto-jet are removed from the list of input objects and the stable proto-jet is added to the list of jets. The whole procedure is repeated until the list is bereft of objects with an E_T above the seed threshold. The cone size and the seed threshold are the parameters of the algorithm.

VI. SMEARING EFFECTS

While a detailed and full-scale detector simulation is beyond the scope of this work, realistic detector effects can easily be approximated. To this end, we smear the generator level information with ECAL and HCAL resolutions of the CMS detector.

For the ECAL resolution function, we use the form

$$\frac{\delta E}{E} = \frac{a}{\sqrt{E}} \oplus \frac{a_n}{E} \oplus C, \quad (6)$$

where a denotes the stochastic term, a_n is the white noise term, and C is the constant term, with the three contributions being added in quadrature. For each of these terms, we use values identical to those for the electromagnetic calorimeter of the CMS [30], namely

$$C = 0.55\%,$$

$$a_n = \begin{cases} 2.1 \times 10^{-3} \text{ GeV} & |\eta| < 1.5 \\ 2.45 \times 10^{-3} \text{ GeV} & 1.5 \leq |\eta| \leq 2.5 \end{cases}$$

$$a = \begin{cases} 2.7 \times 10^{-2} \text{ GeV}^{1/2} & |\eta| < 1.5 \\ 5.7 \times 10^{-2} \text{ GeV}^{1/2} & 1.5 \leq |\eta| \leq 2.5 \end{cases}$$

The resolutions for $\Delta\eta$ and $\Delta\phi$ were taken to be 0.02 and 0.001, respectively, for both the barrel and the endcaps.

For the hadronic calorimeter, the resolutions were once again assumed to be the same as those for the CMS HCAL [38,39],³ namely,

(i) Barrel:

$$\frac{\delta E}{E} = \frac{65\%}{\sqrt{E/\text{GeV}}} \oplus 5\%, \quad \Delta\eta = 0.04, \quad \Delta\phi = 0.02,$$

²The seed threshold can vary from 0.5 to 2.0 GeV depending on the energy of reconstructed jet.

³Reference [38] is an internal document of CMS collaboration and hence not available for outside the physics community.

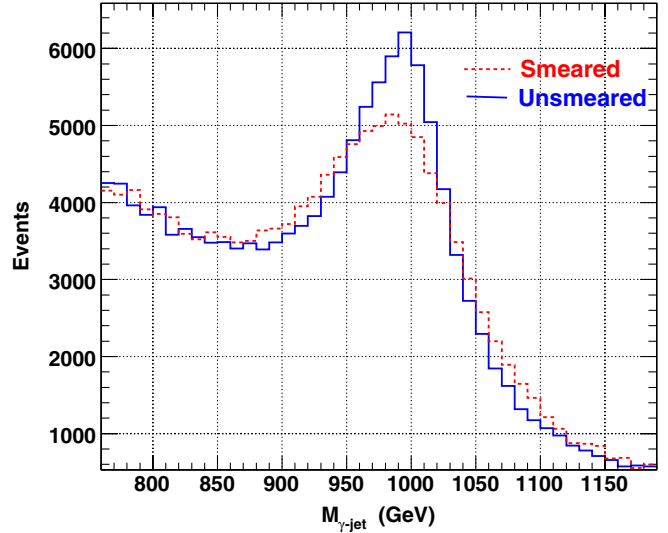


FIG. 6 (color online). Effect of smearing on the mass peak for an excited quark of 1 TeV.

(ii) Endcaps:

$$\frac{\delta E}{E} = \frac{83\%}{\sqrt{E/\text{GeV}}} \oplus 5\%, \quad \Delta\eta = 0.03, \quad \Delta\phi = 0.02,$$

(iii) Forward region:

$$\frac{\delta E}{E} = \frac{100\%}{\sqrt{E/\text{GeV}}} \oplus 5\%, \quad \Delta\eta = 0.04, \quad \Delta\phi = 0.04.$$

The four momenta of the photon and jet were recalculated after applying these resolution effects using an appropriate Gaussian smeared function. In Fig. 6, we show the effect of resolution on the mass peak for a M_{q^*} of 1 TeV.

VII. KINEMATICAL VARIABLES

In Fig. 7, we show the kinematical distributions for the leading photon and the leading jet for $P_T^{\gamma, \text{jet}} \geq 200$ GeV data set for the background and the signal for $M_{q^*} = 1$ TeV. For the purpose of visual clarity, the distributions for $Z + \gamma$ and $W + \gamma$ backgrounds have been scaled up by a factor of 10. The bump in the transverse momentum distributions [Figs. 7(a) and 7(b)] are primarily driven by the on shell production of the q^* and, therefore, are centered slightly below $M_{q^*}/2$. While the dissimilar natures of the P_T^{jet} and P_T^γ distributions for the QCD-dijet background may seem intriguing, this is but a manifestation of the fact that no isolation criteria for the photon has been imposed so far. A dijet event can manifest itself as a photon + jet candidate if one of them leads to a sufficiently high and well-collimated deposition in the ECAL with the rest of the energy being deposited in the form of unclustered objects. With the probability of this happening being a function of

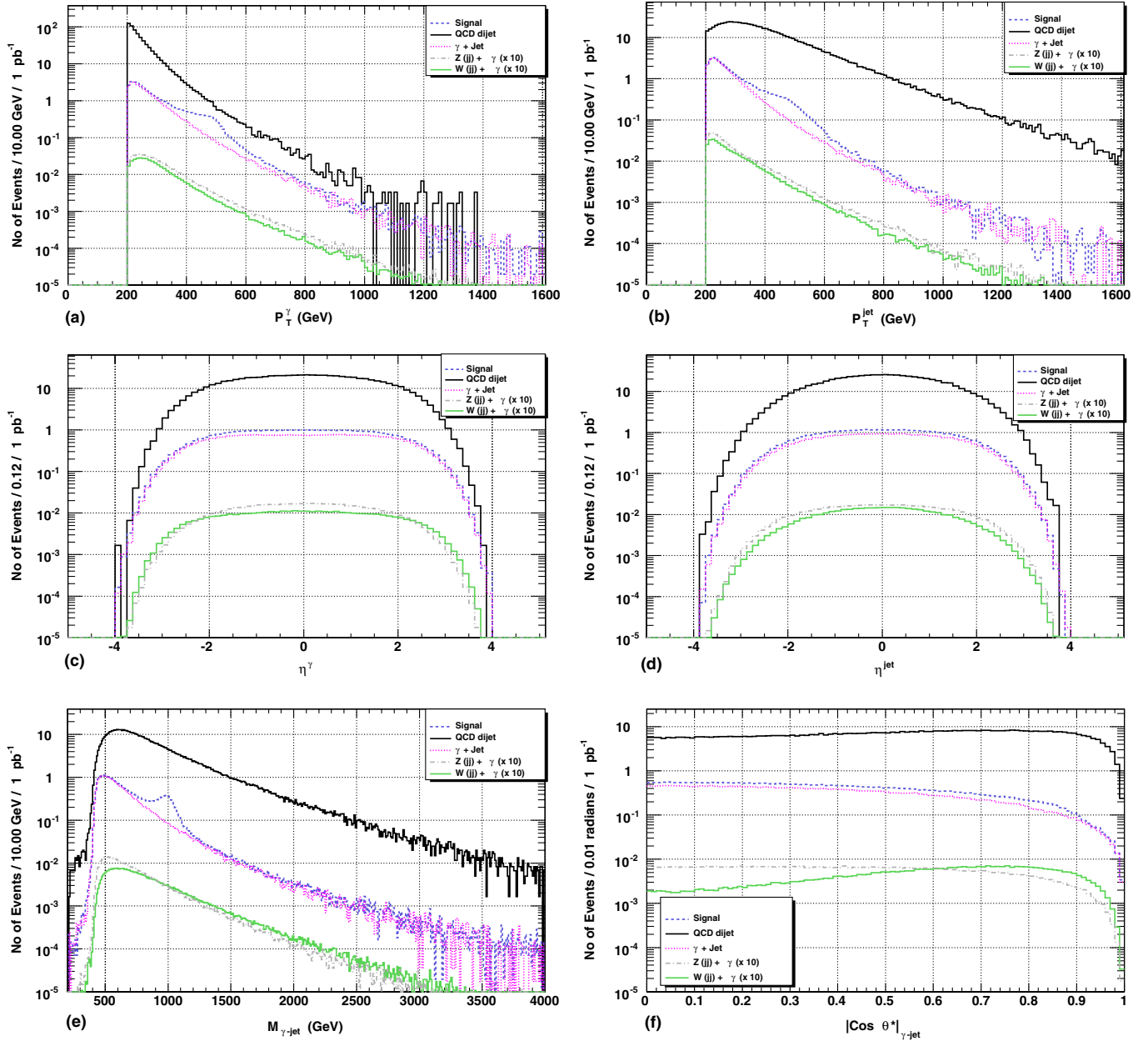


FIG. 7 (color online). Kinematic variable distributions for leading photon and jet after 200 GeV preselection cut on P_T and without isolation requirements (a) P_T^γ distribution, (b) P_T^{jet} distribution, (c) η^γ distribution, (d) η^{jet} distribution, (e) $M_{\gamma\text{-jet}}$ distribution, and (f) $|\cos\theta^*|_{\gamma\text{-jet}}$. The signal corresponds to $M_{q^*} = 1$ TeV.

the original parton energy, it is understandable that the two distributions are different. Note that, once isolation criteria are imposed, most such photon candidates would disappear.

As is evident from Fig. 7(e), an excess in the invariant mass spectrum would be quite prominent for even $\int L \cdot dt = 1 \text{ pb}^{-1}$. The t -channel contribution has been included and manifests itself in the elongation of the side bands. It may be noted that the QCD dijet background is more than 10 times as large as the signal, but falls very rapidly with $P_T^{\gamma/\text{jet}}$ (the mistagging probability has already been included).

Figure 7(f) shows the distribution in the subprocess center of mass scattering angle, with $\cos\theta^* = \tanh[(\eta^\gamma - \eta^{\text{jet}})/2.0]$. Note that major differences between the signal and background profile occur only for p_T and invariant mass distributions, whereas the other phase space variables are not very sensitive discriminants.

Figure 8 shows similar distributions as in Fig. 7 but for the $M_{q^*} = 5$ TeV point instead. For these distributions we have used a $P_T^{\gamma/\text{jet}}$ cut of 1 TeV at the preselection level. With the P_T spectrum for the photon from QCD background falling very rapidly, the signal dominates over the background above 2 TeV even without isolation cuts. As

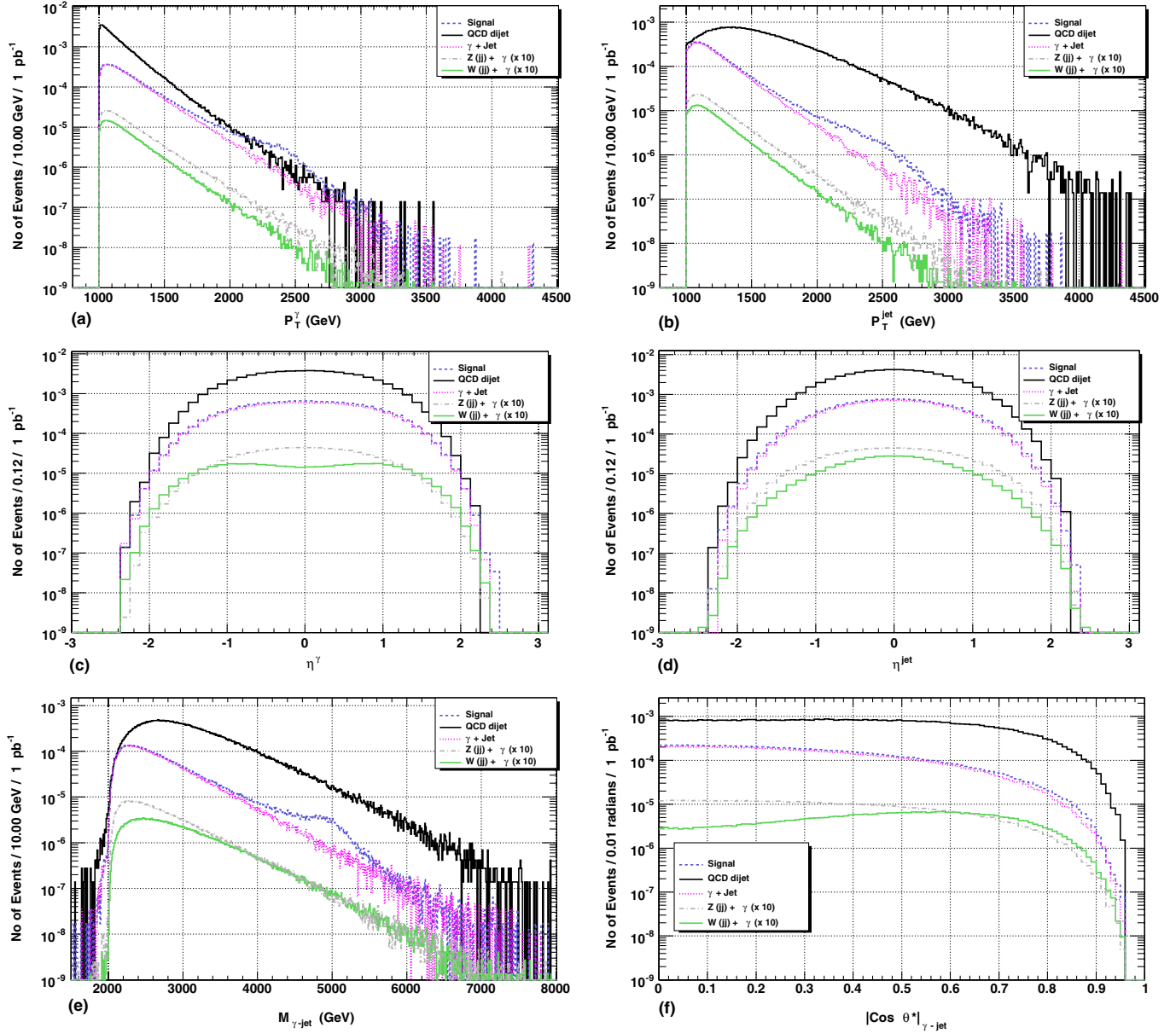


FIG. 8 (color online). As in Fig. 7 but with a 1 TeV preselection cut on P_T and a signal corresponding to $M_{q^*} = 5$ TeV instead.

for the corresponding invariant mass ($M_{\gamma\text{-jet}}$) distribution—see Fig. 8(e)—a combination of the large natural width and smearing effects results in a broad bump rather than a sharp one. Once again, the other distributions do not discriminate between the signal and background in any forceful manner. While the slight dip in the central η^γ region for the $W + \gamma$ process might seem intriguing (especially in the absence of any such dip in the $Z + \gamma$ distribution), it is but a straightforward reflection of the well-known radiation-amplitude-zero (RAZ) present in the former [40,41]. That the RAZ in the angular distribution is apparent only for the high $P_T^{\gamma,\text{jet}}$ cutoff case can be understood by realizing that the rapidity of the photon as measured in the laboratory can be related to the rapidity

(scattering angle) in the partonic subprocess center of mass frame through $\eta(\gamma) = \ln\sqrt{x_1/x_2} + \eta^*(\gamma)$ where x_i are the momentum fractions of the incoming partons. For small \hat{s} values (hence lower CKIN(3) cuts), the parton densities are maximized when the (anti)quark acquire small (large) momentum fractions, respectively. This leads to a considerably large contribution to η^γ from the boost, thereby smearing the original double peaked η^γ distribution into a centrally peaked one. On the contrary, for typically high \hat{s} (CKIN(3) ≥ 1 TeV) values the x_i tend to be not too different thereby reducing the smearing on this account.

In Table III we show the preselection efficiencies and geometrical acceptances for the CMS detector for various

TABLE III. Preselection efficiency and geometrical acceptance along with statistical errors for various SM backgrounds and a few signal points.

Selection cut	Signal		$\gamma + \text{Jet}$	QCD	$Z + \gamma$	$W + \gamma$
	Mass	%				
$P_T^{\gamma, \text{jet}} \geq 200 \text{ GeV}$	[1 TeV]	48.69 ± 0.08	44.22 ± 0.09	0.900 ± 0.014	38.39 ± 0.09	37.14 ± 0.09
$P_T^{\gamma, \text{jet}} \geq 500 \text{ GeV}$	[4 TeV]	40.19 ± 0.05	39.80 ± 0.09	0.415 ± 0.007	50.43 ± 0.10	50.57 ± 0.10
$P_T^{\gamma, \text{jet}} \geq 1 \text{ TeV}$	[5 TeV]	47.43 ± 0.07	46.02 ± 0.10	0.510 ± 0.008	58.84 ± 0.11	59.97 ± 0.11
$ \eta^\gamma \leq 2.5, \eta^{\text{jet}} \leq 3.0,$	[1 TeV]	42.41 ± 0.07	38.19 ± 0.09	0.813 ± 0.013	32.81 ± 0.08	33.22 ± 0.08
$ \eta^\gamma \notin [1.4442, 1.5666]$	[4 TeV]	38.23 ± 0.05	37.83 ± 0.08	0.398 ± 0.007	47.42 ± 0.10	48.42 ± 0.10
	[5 TeV]	46.42 ± 0.07	45.04 ± 0.07	0.503 ± 0.008	56.39 ± 0.11	58.74 ± 0.11

backgrounds and signal of $M_{q^*} = 1, 4,$ and 5 TeV against the total generated events.

VIII. ISOLATION VARIABLES

In a detector, a photon candidate is reconstructed by summing the energy deposition in ECAL towers in a limited region of space, with the sum required to be above a certain E_T threshold. For the sake of simplicity, this limited region can be visualized as a cone in $\Delta\eta - \Delta\phi$ space given by $\Delta R \equiv \sqrt{\Delta\phi^2 + \Delta\eta^2}$ and containing most of the energy of the electromagnetic object.

A jet fragmenting into neutral and charged hadrons with a $\pi^0/\eta/\rho/\omega \rightarrow \gamma\gamma$ (with overlapping photons) carrying maximum momentum can also lead to fake single-photon candidates. To remove such events, photons are required not to have associated charged tracks within a cone of size R_{iso} . This is implemented by requiring that the scalar/vector sum of energy/transverse momentum of the charged tracks within R_{iso} should be below a certain threshold. For example, the D0 and the CDF experiments demand that the E_T due to charged tracks within a cone of $\Delta R = 0.4$ around the photon should be less than a certain value. In this analysis, we closely follow the CMS detector simulation studies [42] and consider the following isolation variables:

- (i) the number of tracks (N_{trk}) above a certain threshold inside a cone around the photon candidate.
- (ii) the scalar sum of transverse energy ($E_{T\text{SUM}}$) inside a cone around the photon. Although in a full detector simulation the $E_{T\text{SUM}}$ is measured separately for ECAL and HCAL, when working at the generator level, we combine them into a single variable taking into account all electromagnetic and hadronic objects around the photon in a particular cone.

A. Track isolation

For the purpose of track isolation, only “stable” charged particles such as $\pi^\pm, K^\pm, e^\pm,$ and P^\pm are considered. With π^\pm alone contributing more than 80% of all charged tracks, the other contributions are negligible. Figure 9 shows the distribution of the number of charged tracks (N_{trk}) around the leading photon in a cone of size $\Delta R \leq 0.35$ for a $M_{q^*} = 1 \text{ TeV}$ signal as well as for the total background. Since the leading photon is the *true* photon

for signal events, most of them are associated with zero tracks ($N_{\text{trk}} = 0$) and the distribution falls off very rapidly for larger N_{trk} values. For background events, though, the distribution peaks at $N_{\text{trk}} \sim 7-8$ and then falls slowly. The small rise at $N_{\text{trk}} = 0$ is due to the fact that $\gamma + \text{jet}(\text{SM})$ and $W/Z + \gamma$ backgrounds have true photons as the leading photon in the event and have no tracks around them, while the rising part along with the extended tail is mainly contributed by the QCD dijet events where the fake photon typically has a large number of tracks around itself. In this study, we accept a photon to be an isolated one if there is no track with minimum transverse momentum ($P_{T\text{min}}^{\text{trk}}$) within a given cone around it. It should be noted that comparative distributions of signal and total background, as shown in Fig. 9, are not overly sensitive to moderate changes in the $P_{T\text{min}}^{\text{trk}}$ value (the exact values are discussed at a later stage).

Each event at the LHC would typically be accompanied by a large number of tracks (with energies in the range of a few MeVs to a few GeVs) arising primarily from minimum bias and underlying events as well as from ISR and FSR. The close proximity of such tracks to direct photons could seemingly render the latter nonisolated. To avoid losing such candidates, tracks are usually required to pass certain

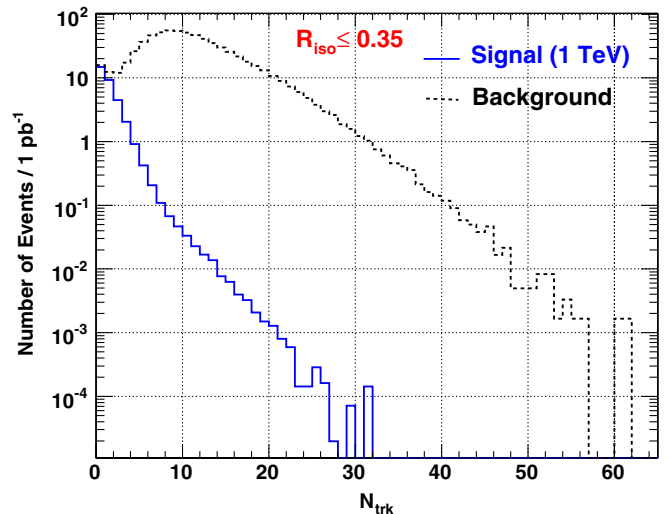


FIG. 9 (color online). Number of tracks (N_{trk}) for the signal ($M_{q^*} = 1 \text{ TeV}$) and the background events around the photon.

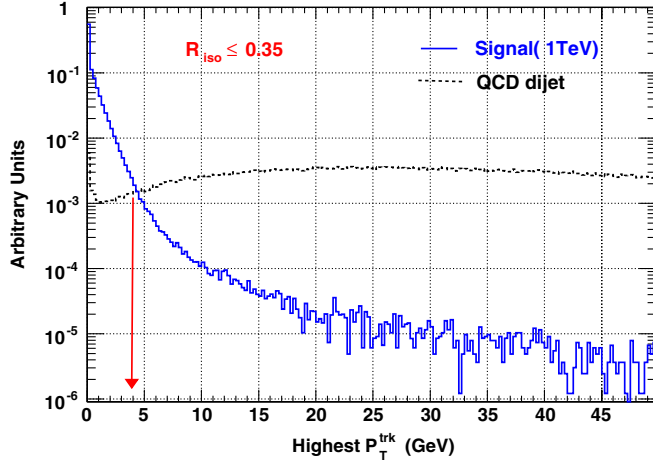


FIG. 10 (color online). Highest P_T track around the leading photon for the signal and the QCD dijet background (a) $M_{q^*} = 1$ TeV. An isolation cone of size 0.35 has been used. Both distributions are normalized to unity for the sake of comparison.

criteria. Using $P_{T\min}^{\text{trk}}$ as one such criterion [29,42,43], we examine both the signal and the QCD dijet background in terms of the distribution for the highest- P_T track. As is evident from Fig. 10, any tracks accompanying the photon in a signal event tend to have a low P_T , whereas for the background events, the distribution is a very wide one. An indicative value for the optimal $P_{T\min}^{\text{trk}}$ is given by the point of intersection of the two normalized distributions (~ 4 GeV in Fig. 10). Thus, counting only those tracks around the photon with $P_T^{\text{trk}} > 4$ GeV, a requirement of $N_{\text{trk}} = 0$ in the isolation cone would retain a large fraction of the signal while rejecting the bulk of the background.

Noting that the optimal value of the $P_{T\min}^{\text{trk}}$ also depends on signal profile (e.g., for 5 TeV mass states it is about 6 GeV), in Fig. 11, we display the consequent interplay between signal efficiency and the signal to background ratio (S/B) for different $P_{T\min}^{\text{trk}}$ values, for two different signal points ($M_{q^*} = 1$ TeV and 5 TeV). It is evident from the distributions that adopting a higher threshold would remarkably increase the signal efficiency with only a small loss in the S/B ratio. More importantly, the track isolation requirement reduces the fake photon events with the major effect showing up in the QCD dijet background. As is obvious, the strict requirement of $N_{\text{trk}} = 0$ in a given cone around the photon reduces only a small fraction of the signal whereas the S/B ratio is improved considerably.

To keep the analysis simple, we then dispense with an M_{q^*} -dependent choice of the threshold, and instead demand $P_{T\min}^{\text{trk}} = 3$ GeV and $N_{\text{trk}} = 0$ irrespective of the mass of the q^* being looked for. Although a choice of $P_{T\min}^{\text{trk}} = 4$ GeV would have led to better results (see Fig. 9), we make a more conservative choice to account for the fact that, in a real detector, the tracking efficiency is usually less than 100%.

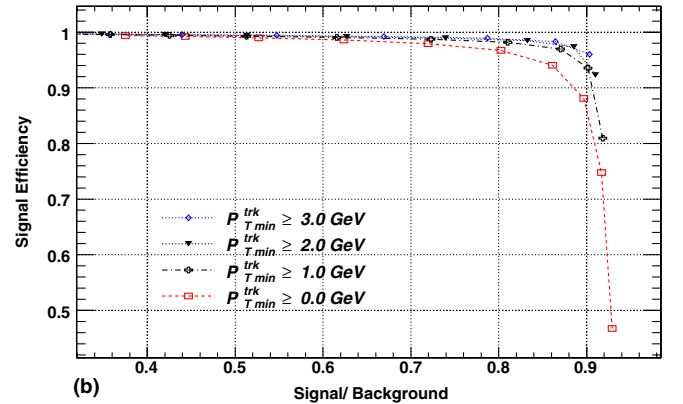
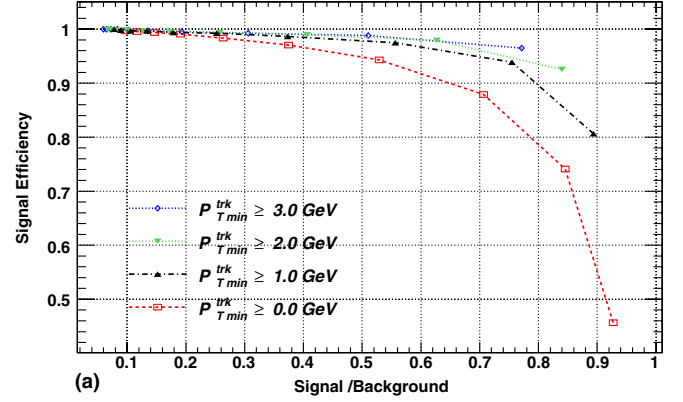


FIG. 11 (color online). Effect of $P_{T\min}^{\text{trk}}$ choice on signal efficiency vs S/B for the photons from (a) 1 TeV signal, (b) 5 TeV signal. For a given threshold ($P_{T\min}^{\text{trk}}$), the individual points correspond to differing values of the number of tracks, N_{trk} , allowed in a cone starting with 0 tracks (for the rightmost point) and increasing in steps of one.

B. E_T sum isolation

In this subsection, we analyze another isolation variable, namely, the scalar sum of transverse energy inside a cone around the photon. Figure 12 shows the $E_{T\text{SUM}}$ distribution for the leading photon for $M_{q^*} = 1$ TeV for a cone of size

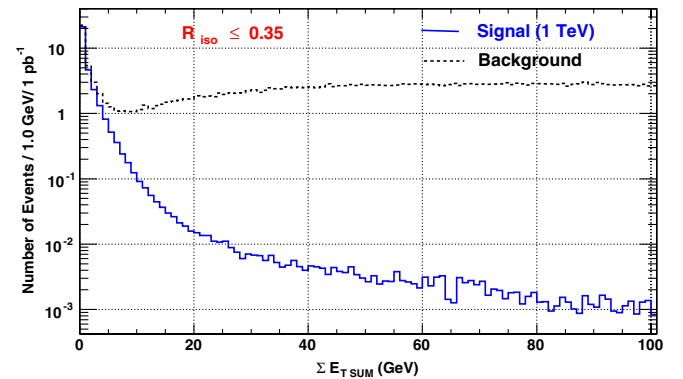


FIG. 12 (color online). $E_{T\text{SUM}}$ for the background and the signal events around photons for (a) $M_{q^*} = 1$ TeV. Distributions are normalized for $\int L dt = 1 \text{ pb}^{-1}$.

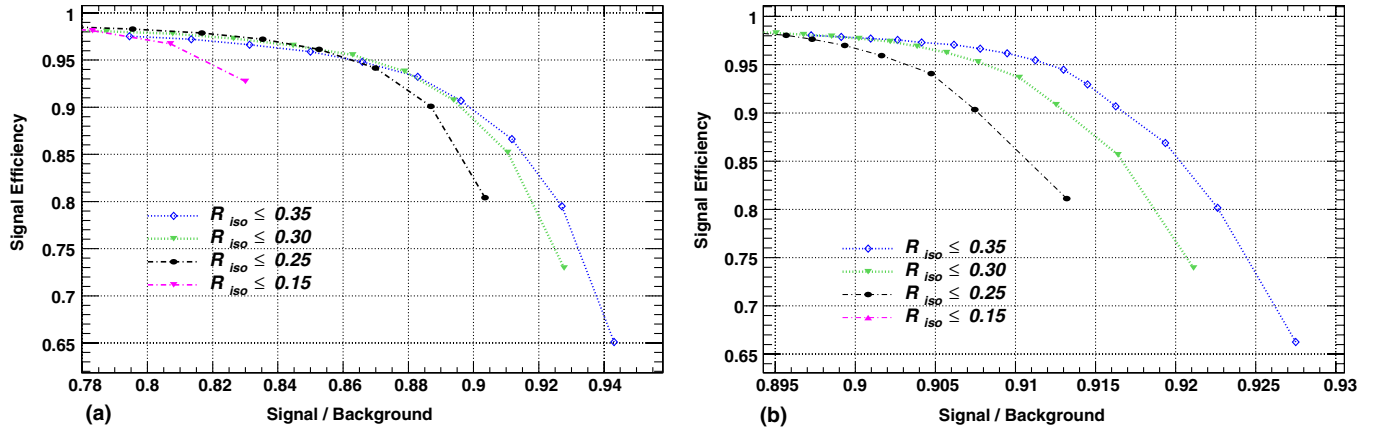


FIG. 13 (color online). Signal efficiency vs S/B ratio for different cone sizes for different choices of the $E_{T\SUM}$ threshold around the leading photon for (a) $M_{q^*} = 1$ TeV and (b) $M_{q^*} = 5$ TeV. For each choice of the cone size, individual points correspond to a particular choice for the $E_{T\SUM}$ threshold in that cone, starting with 1 GeV at the rightmost point and going up in steps of 1 GeV.

$\Delta R = 0.35$. It is evident that a large fraction of signal events have $E_{T\SUM} < 5.0$ GeV whereas the background events generically have $E_{T\SUM} \geq 5$ GeV.

Figures 13(a) and 13(b), respectively, show the signal efficiency vs the S/B ratio for 1 TeV and 5 TeV signal

points. It is evident that, for a given signal efficiency, a higher S/B ratio can be attained for larger cone sizes. For example, demanding $\Delta R \leq 0.35$ leads to a large signal efficiency ($\sim 92\%$) and $S/B > 0.88$ for either choices of M_{q^*} . On the other hand, any relaxation beyond $E_{T\SUM} >$

TABLE IV. Fraction of events surviving for the signal and various backgrounds with statistical errors for different isolation cuts (after P_T cut).

R_{iso}	N_{trk}	P_{Tmin}^{trk} (GeV)	$E_{T\SUM}^{max}$ (GeV)	S (%)	QCD (%)	$\gamma + \text{Jet}$ (%)	Z + γ (%)	W + γ (%)	(S/B)
$M_{q^*} = 1.0$ TeV									
0.30	0	1.0	5.0	73.56 ± 0.13	0.93 ± 0.01	72.92 ± 0.18	75.00 ± 0.20	71.89 ± 0.19	0.970
			6.0	73.70 ± 0.13	0.94 ± 0.01	73.07 ± 0.18	75.13 ± 0.20	72.02 ± 0.19	0.967
		2.0	5.0	81.24 ± 0.14	1.12 ± 0.02	80.55 ± 0.19	82.89 ± 0.21	79.42 ± 0.20	0.951
			6.0	81.67 ± 0.14	1.15 ± 0.02	80.99 ± 0.19	83.34 ± 0.21	79.85 ± 0.20	0.946
		3.0	5.0	83.00 ± 0.14	1.19 ± 0.02	82.33 ± 0.19	84.81 ± 0.21	81.21 ± 0.21	0.941
			6.0	83.73 ± 0.14	1.25 ± 0.02	83.08 ± 0.19	85.57 ± 0.22	81.93 ± 0.21	0.930
0.35	0	1.0	5.0	69.84 ± 0.13	0.82 ± 0.01	69.29 ± 0.18	71.15 ± 0.19	68.24 ± 0.19	0.984
			6.0	70.05 ± 0.13	0.83 ± 0.01	69.50 ± 0.18	71.38 ± 0.19	68.45 ± 0.19	0.982
		2.0	5.0	79.04 ± 0.14	1.01 ± 0.02	78.40 ± 0.19	80.53 ± 0.21	77.23 ± 0.20	0.967
			6.0	79.77 ± 0.14	1.05 ± 0.02	79.14 ± 0.19	81.35 ± 0.21	77.97 ± 0.20	0.960
		3.0	5.0	81.00 ± 0.14	1.08 ± 0.02	80.39 ± 0.19	82.63 ± 0.21	79.21 ± 0.20	0.957
			6.0	82.15 ± 0.14	1.14 ± 0.02	81.57 ± 0.19	83.91 ± 0.21	80.38 ± 0.21	0.947
$M_{q^*} = 5.0$ TeV									
0.30	0	1.0	5.0	82.92 ± 0.15	1.82 ± 0.02	83.07 ± 0.19	83.31 ± 0.17	81.62 ± 0.17	0.955
			6.0	83.07 ± 0.15	1.83 ± 0.02	83.20 ± 0.19	83.46 ± 0.17	81.75 ± 0.17	0.954
		2.0	5.0	91.05 ± 0.10	2.11 ± 0.02	91.11 ± 0.20	91.45 ± 0.17	89.50 ± 0.17	0.950
			6.0	91.51 ± 0.15	2.14 ± 0.02	91.55 ± 0.20	91.92 ± 0.10	89.93 ± 0.18	0.950
		3.0	5.0	92.90 ± 0.15	2.17 ± 0.02	92.98 ± 0.20	93.39 ± 0.18	91.32 ± 0.18	0.949
			6.0	93.67 ± 0.15	2.22 ± 0.02	93.72 ± 0.20	94.18 ± 0.18	92.07 ± 0.18	0.947
0.35	0	1.0	5.0	78.82 ± 0.14	1.63 ± 0.02	79.01 ± 0.19	79.31 ± 0.16	77.68 ± 0.16	0.960
			6.0	79.04 ± 0.10	1.64 ± 0.02	79.22 ± 0.19	79.52 ± 0.16	77.90 ± 0.16	0.960
		2.0	5.0	88.57 ± 0.15	1.94 ± 0.02	88.65 ± 0.20	89.01 ± 0.17	87.16 ± 0.17	0.956
			6.0	89.34 ± 0.15	1.97 ± 0.02	89.40 ± 0.20	89.77 ± 0.17	87.92 ± 0.17	0.956
		3.0	5.0	90.64 ± 0.15	1.99 ± 0.02	90.72 ± 0.20	91.12 ± 0.17	89.24 ± 0.17	0.955
			6.0	91.85 ± 0.15	2.04 ± 0.02	91.91 ± 0.20	92.35 ± 0.18	90.45 ± 0.18	0.954

TABLE V. Number of events surviving for the $M_{q^*} = \Lambda = 1$ TeV signal and the backgrounds for $\int L dt = 100 \text{ pb}^{-1}$ for different isolation cuts.

R_{iso}	N_{trk}	$P_{T \text{ min}}^{\text{trk}}$ (GeV)	$E_{T \text{ SUM}}^{\text{max}}$ (GeV)	S	QCD	$\gamma + \text{Jet}$	$Z + \gamma$	$W + \gamma$	Tot. background	(S + B)
0.30	0	1.0	5.0	2734	626.2	2185	4.10	2.97	2818	3368
			6.0	2740	634.4	2190	4.11	2.98	2831	3381
		3.0	5.0	3085	803.0	2467	4.64	3.36	3278	3896
			6.0	3112	845.9	2490	4.68	3.39	3344	3966
0.35	0	1.0	5.0	2596	554.0	2076	3.89	2.82	2637	3157
			6.0	2604	560.8	2083	3.91	2.83	2650	3172
		3.0	5.0	3011	727.4	2409	4.52	3.28	3144	3747
			6.0	3054	772.1	2444	4.59	3.32	3224	3834

5.0 GeV reduces S/B considerably with only a very small gain in signal efficiency. Several $E_{T \text{ SUM}}$ thresholds for different cone sizes were analyzed along with track isolation requirements to optimize signal efficiency along with the S/B ratio.

C. Final selection cuts

In Table IV, we show the efficiencies for signal and background for all the isolation variables with differing thresholds. Since we aim to observe any excess as a mass peak over the SM continuum and, in the early phase of the LHC operation, would be able to identify a signal only for low masses, it is rather important to have a large signal efficiency and S/B ratio for smaller M_{q^*} . Hence we have used the isolation criteria befitting a 1 TeV signal point (note that this also works reasonably for higher M_{q^*} s), and performed this analysis for all the different signal points considered in this study. Note that, while it is indeed possible to have yet other criteria to select different threshold based on real detector simulation, the qualitative differences in the results are small.

Based on these studies, the final selection cuts applied are as follows (the $P_T^{\gamma, \text{jet}}$ requirements being determined by the range of M_{q^*} being investigated, vide Sec. IV):

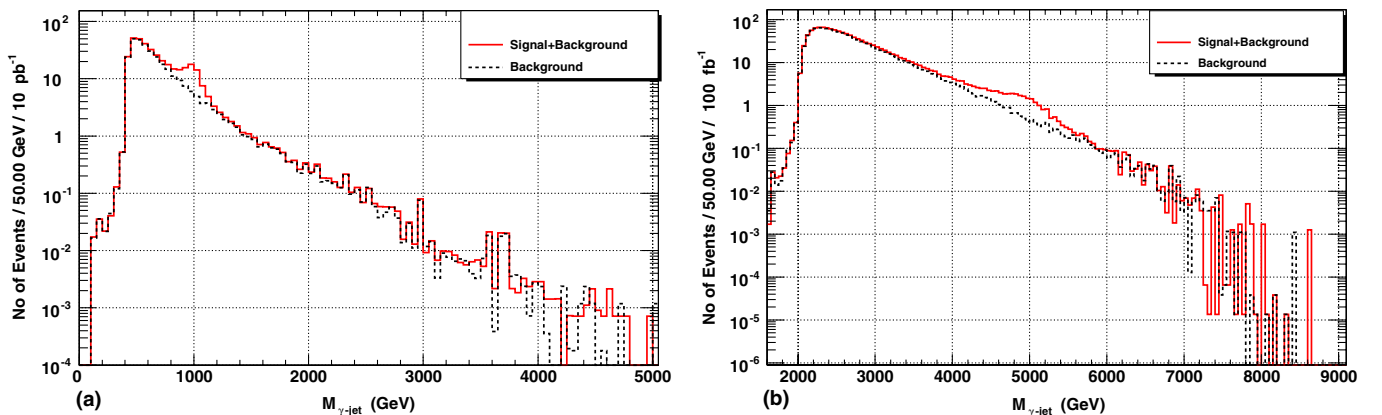
- (i) $P_T^{\gamma}, P_T^{\text{jet}} \geq 200$ GeV (500 GeV, 1 TeV);
- (ii) $|\eta^{\gamma}| \leq 2.5$ & $|\eta^{\text{jet}}| \notin [1.4442, 1.5666]$;
- (iii) $|\eta^{\text{jet}}| \leq 3.0$;
- (iv) $N_{\text{trk}} = 0$ for $P_T^{\text{trk}} \geq 3.0$ GeV within $R_{\text{iso}} \leq 0.35$;
- (v) $E_{T \text{ SUM}} < 5.0$ GeV within $R_{\text{iso}} \leq 0.35$.

In Table V, we show the expected number of events for $M_{q^*} = \Lambda = 1$ TeV for an integrated luminosity of 100 pb^{-1} for various combinations of isolation variables discussed above.

In Fig. 14 we have shown the invariant mass distribution for both signal + background (S + B) and background (B) after the all selection cuts.

IX. SIGNIFICANCE LEVEL

For reporting a discovery significance, we adopt a frequentist Monte Carlo technique based on a method of hypothesis testing originally due to Neyman and Pearson [29,44,45]. The aim is to determine which one of two


 FIG. 14 (color online). Invariant mass of γ -jet system for signal + background and background after all the isolation and kinematical cuts. (a) $M_{q^*} = 1$ TeV, (b) $M_{q^*} = 5$ TeV.

competing hypotheses, the so-called null hypothesis (H_0) and the alternative hypothesis (H_1) is favored by the data. In the present context, the SM only case (background) constitutes the null hypothesis (H_0) and the presence of new physics (i.e. excited quark contribution to the final state) along with the SM is the alternative hypothesis (H_1). Heretofore, H_0 and H_1 will also be referred to as background only (B) and signal plus background (S + B) hypotheses.

In the Neyman-Pearson method one aims to design a test which minimizes the probability β of erroneously rejecting an alternative hypothesis when it is actually true. Understandably, $1 - \beta$ is defined as the power of a test and the most powerful (MP) test is the one which maximizes the power for a given value of the probability α of rejecting the null hypothesis as false, when it is true instead. According to the Neyman-Pearson lemma [44], the condition for the MP test is obtained as a condition on the log likelihood ratio (LLR) of a given data set coming from the null or the alternative hypothesis. Even when a MP test does not exist, the LLR statistic can be used for testing between two hypotheses due to its statistically desirable properties [46]. One accepts or rejects H_0 based on the value of the LLR computed from the data. If the value of the LLR falls within a range of values (the critical region) which is unlikely to come from H_0 then H_0 is rejected. Now, α as defined above is clearly the probability of the LLR value falling in the critical region when H_0 is true. Hence, $1 - \alpha$ is reported as the significance level of rejecting H_0 (i.e., the SM in our case), or, in other words, this is the discovery confidence level.

In general, a LLR test can be constructed out of one or many discriminating quantities (e.g. P_T , angular separation, etc.). In this analysis, the LLR has been constructed out of a single discriminating variable, namely $M_{\gamma\text{-jet}}$, the invariant mass of the leading γ and jet. While this is obviously the most sensitive discriminant in the case of

on shell production, it plays an important role even for virtual exchanges [25].

The likelihood ratio is defined as the ratio of Poisson probabilities:

$$Q = \frac{P_{\text{Pois}}(\text{data}|S + B)}{P_{\text{Pois}}(\text{data}|B)},$$

$$P_{\text{Pois}}(\text{data}|S + B) \equiv (s_i + b_i)^{n_i} e^{-(s_i + b_i)} / n_i!,$$

$$P_{\text{Pois}}(\text{data}|B) \equiv (b_i)^{n_i} e^{-b_i} / n_i!, \quad (7)$$

where $s_i + b_i$ are the number of events expected in the i^{th} bin of the $M_{\gamma\text{-jet}}$ histogram according to the S + B hypothesis whereas b_i corresponds to the B hypothesis. n_i here denotes the number of events in the i^{th} bin of the $M_{\gamma\text{-jet}}$ histogram from “data.” All efficiencies are to be folded in s_i , b_i , and n_i .

The LLR statistic is then given by the expression

$$-2 \ln Q = 2 \sum_{i=1}^{n_{\text{bins}}} [s_i - n_i \ln(1 + s_i/b_i)]. \quad (8)$$

The data n_i in the i^{th} bin of the test variable is generated as a random Poisson fluctuation around the mean value of the i^{th} bin of the theoretical $M_{\gamma\text{-jet}}$ histogram.

The significance level is defined as

$$\alpha = 1 - CL_B = P(Q \leq Q_{\text{obs}}|B), \quad (9)$$

the fraction of experiments in a large ensemble of background only experiments which would produce results more signal-like than the observed data. By definition, a S + B hypothesis is “confirmed” at the 5σ (3σ) level if $\alpha < 2.8 \times 10^{-7}$ (1.35×10^{-3}) [47].

In Fig. 15, we show the LLR distribution for S + B and B type hypotheses for two different mass points. The luminosities have been chosen so as to yield a 5σ significance for the S + B hypothesis. We have used 10^7 MC trials for these distributions. In this figure, $1 - CL_B$ is the

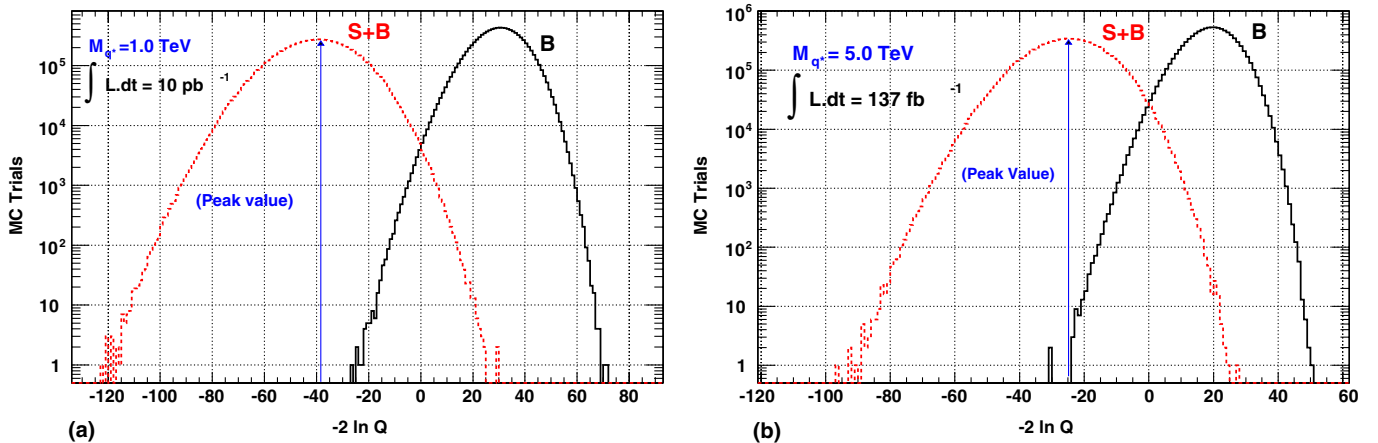


FIG. 15 (color online). Log likelihood ratio distributions for S + B and B type hypotheses for a 5σ significance for (a) 1.0 TeV, (b) 5.0 TeV q^* states.

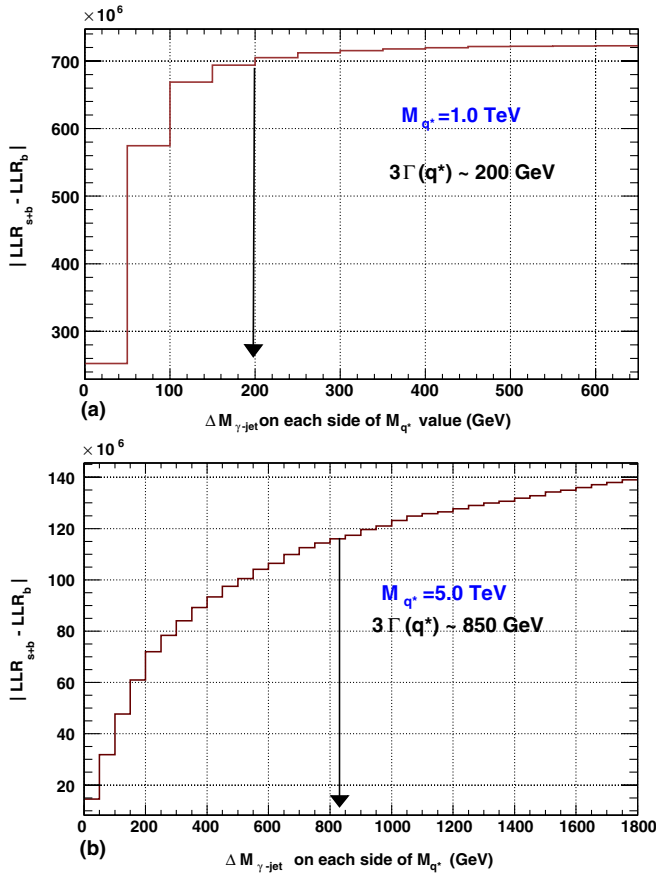


FIG. 16 (color online). Effective LLR contribution as a function of $\Delta M_{\gamma\text{-jet}}$ on each side of q^* state of mass (a) 1.0 TeV and (b) 5.0 TeV.

fraction of MC trials of background type hypothesis which falls to the left side of the peak value of LLR_{S+B} .

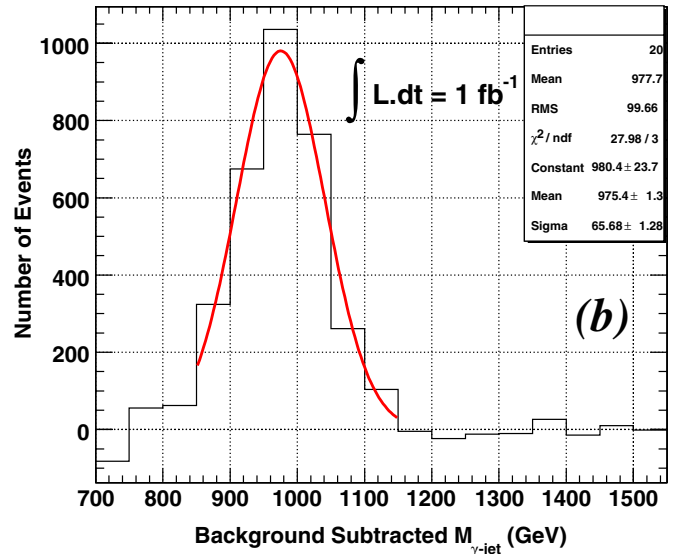
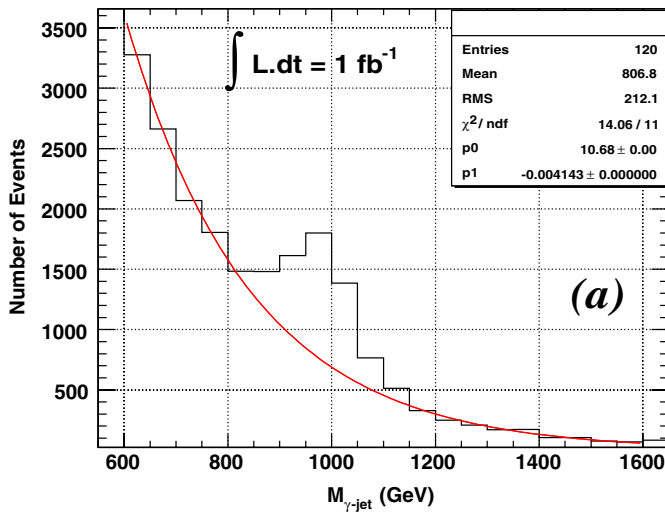


FIG. 17 (color online). (a) Background fit on the $(S+B)$ distribution with an exponential function for 1.0 TeV q^* for an integrated luminosity of 1 fb^{-1} . (b) The corresponding background subtracted invariant mass distribution.

In Fig. 16 we show the functional dependence of the LLR discriminator on the width of the mass window chosen around M_{q^*} . As is apparent from the figure, beyond $\pm 3\Gamma(q^*)$ the two hypotheses look similar and hence the LLR test does not contribute to the significance level. We find similar results for all signal points and, hence, for the final selection we use $M_{q^*} \pm 3\Gamma(q^*)$ as the mass window.

X. BACKGROUND SUBTRACTED INVARIANT MASS

In this section, we describe a procedure to estimate the number of events under the mass peak in the case of a discovery (i.e. if the data supports the $S+B$ hypothesis). Assuming an excess centered approximately around $M_{\gamma\text{-jet}} = M_0$, the first step constitutes fitting the data over an $M_{\gamma\text{-jet}}$ range centered around M_0 but much wider than the region of the excess, the aim being to fit the background as well as the sidebands. While in a real experiment one would attempt to fit the sidebands from data alone, here we use a large MC sample to determine the shape of the sidebands and find that an exponential describes them well (see Fig. 17 for $M_0 = 1 \text{ TeV}$). To generate realistic distributions, we consider $(s+b)$ in each bin to be an independent Poisson distributed (and integer valued) variable with a mean equalling the theoretically expected number of events. A random fluctuation was then used to generate the “experimentally observed” events in the bin concerned. For a good background fit on the $(S+B)$ distribution, an identified excess has clearly to be left out. To this end, we leave out the range $\sim [M_0 - 3\Gamma_0, M_0 + 3\Gamma_0]$ consonant with the binning algorithm where $\Gamma_0 = \Gamma(M_{q^*} = M_0)$. For a χ^2 minimization of the fit, the MINUIT [48] package was used within the ROOT

framework [49]. The fit in Fig. 17(a) was done for an integrated luminosity of 1 fb^{-1} although a 5σ signal significance for $M_{q^*} = 1 \text{ TeV}$ is attainable with only 10 pb^{-1} of data. Figure 17(b) shows the background subtracted mass distribution for $M_{q^*} = 1 \text{ TeV}$. Here we have used a single Gaussian to fit the mass spectrum.

While an integrated luminosity of 1 fb^{-1} for new physics mass measurements would normally be considered meager when compared to the LHC design parameters, it is interesting to consider the physics possibilities with far lower luminosities. To this end, we present, in Fig. 18, analogous distributions for only 10 pb^{-1} . While the fit for the background is, understandably, not as good as in the earlier case, once the validity of an exponential fit is accepted, the background subtracted mass fit is still very convincing. In Fig. 18(b) the number of signal events under the Gaussian fit and within the 800–1200 GeV mass range was found to be 30.5 ± 5.5 (stat). The uncertainty due to error on fitting parameters is found to be at most 4.9 events.

We note in passing that in an actual detector at the LHC the mass peak will have a tail on the lower mass side due to partial containment of showers and fitting this may need a

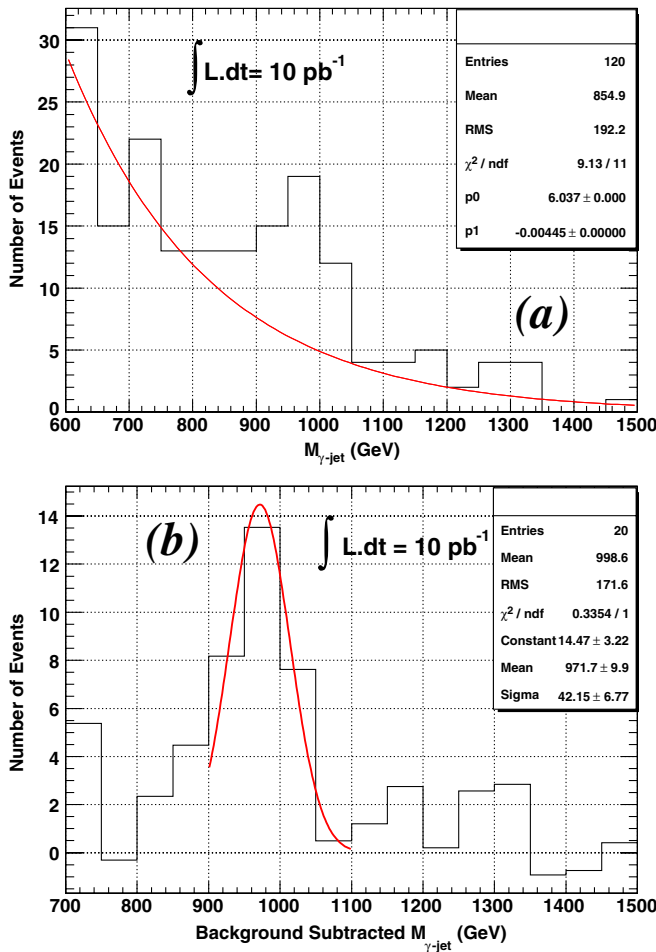


FIG. 18 (color online). As in Fig. 17, but for an integrated luminosity of 10 pb^{-1} instead.

Gaussian modified with a Landau or some other asymmetric distribution thereby broadening the mass peak somewhat.

The invariant mass distribution has two components, the natural Lorentzian part for an unstable particle with a large width and a Gaussian (or a double-Gaussian) distribution due to resolution effects. The combined distribution is a convolution of the two above. Although the combined distribution is thus not a simple one, a single Gaussian fits the mass peak reasonably well and hence we choose to fit the peak with a simple Gaussian.

XI. RESULTS

Figures 19(a) and 19(b), respectively, show the luminosity needed to achieve 5σ (3σ) significance for the signal as a function of the excited quark mass. We find that the

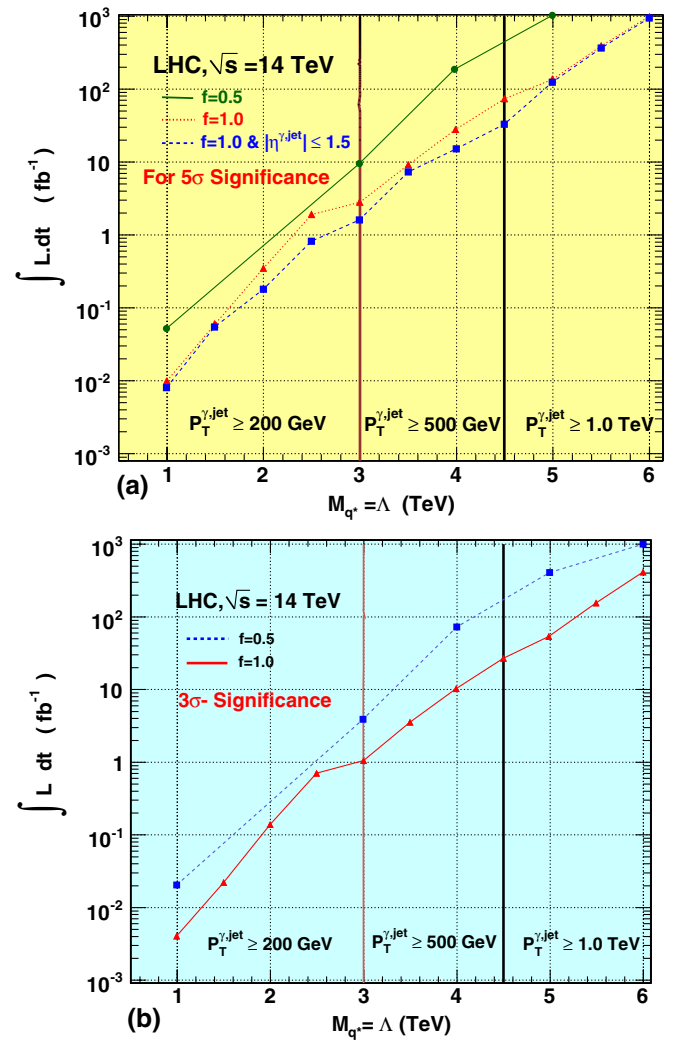


FIG. 19 (color online). Required integrated luminosity as a function of M_{q^*} for (a) 5σ and (b) 3σ significance for two different coupling strengths (systematic uncertainties are not included).

TABLE VI. Cross sections for various M_{q^*} values after imposing all kinematical and isolation cuts.

S.N.	$M_{q^*}^a$ (TeV)	$\Delta M_{\gamma-j}$ $\pm 3\Gamma(q^*)$ (GeV)	$\sigma(S+B)$ (pb)	$\sigma(B)$ (pb)	$\sigma(S^*)^b$ (pb)	Efficiency (S+B) (%)	Efficiency (B) (%)	Efficiency (S*) (%)
1	1.0	800–1200	9.26	4.92	4.34	1.304	0.699	60.28
2	1.5	1200–1800	2.034	1.33	0.694	0.288	0.190	46.71
3	2.0	1600–2400	6.72×10^{-1}	5.10×10^{-1}	1.61×10^{-1}	0.095	0.072	37.23
4	2.5	2000–3000	2.54×10^{-1}	2.10×10^{-1}	4.41×10^{-2}	0.036	0.029	40.67
5	3.0	2450–3550	7.85×10^{-2}	6.44×10^{-2}	1.40×10^{-2}	0.011	0.009	75.95
6	3.5	2900–4150	1.11×10^{-2}	6.93×10^{-3}	4.17×10^{-3}	0.274	0.172	24.70
7	4.0	3300–4700	4.90×10^{-3}	3.40×10^{-3}	1.50×10^{-3}	0.121	0.084	15.60
8	4.5	3700–5300	2.20×10^{-3}	1.57×10^{-3}	6.37×10^{-4}	0.054	0.039	11.48
9	5.0	4150–5850	4.60×10^{-4}	2.47×10^{-4}	2.12×10^{-4}	0.628	0.342	22.49
10	5.5	4500–6450	2.17×10^{-4}	1.29×10^{-4}	8.81×10^{-5}	0.299	0.179	14.91
11	6.0	5000–7000	8.39×10^{-5}	5.14×10^{-5}	3.24×10^{-5}	0.115	0.071	7.85

^aHere $f_1 = f_3 = 1.0$

^bPure new physics contribution evaluated by subtracting B from (S + B)

results obtained using $(-2 \ln Q)$ are consistent with those from the s/\sqrt{b} test statistic. In estimating the required luminosity, we have exploited only the mass peak region of the signal over the SM background. We have used a mass window of $\sim \pm 3\Gamma(q^*)$ around M_{q^*} . In a previous section we have shown that beyond $\pm 3\Gamma(q^*)$ the discriminating statistic, namely, LLR, looks similar for S + B and B.

We have checked the stability of the results by varying the bin width of the invariant mass distribution from 50 GeV to 20 GeV for both $M_{q^*} = 1.0$ TeV and 2.0 TeV and find that the luminosity required for 5σ significance changes by 20% and 1.1%, respectively. For $M_{q^*} = 5.0$ TeV, on the other hand, we varied the bin width from 50 GeV to 100 GeV and found that the required luminosity changes by 2.1%. Similarly we increased the number of Monte Carlo trials by a factor of 10 and found that the

required luminosity changes by $\sim 20\%$, 0.8%, and 2.1%, respectively, for the 1.0, 2.0, and 5.0 TeV mass points.

In Fig. 19(a), corresponding to the $f_i = 1.0$ case, we also demonstrate the effect of restricting the photon and the jet to the central region of the calorimeter on the required luminosity. For 5σ significance, the latter reduces by $\sim 30\%$ up to a mass of 4.5 TeV. For $M_{q^*} = 5.0$ TeV, though, the signal events are mostly produced in the central region and hence the requirement $|\eta^{\gamma, \text{jet}}| \leq 1.5$ does not affect the final result significantly. It is also shown that within the model of compositeness presented here, for $M_{q^*} \gtrsim 5.5$ TeV, a 5σ significance cannot be achieved at a center of mass energy of 14 TeV. While this might seem to run counter to previous work [50], note that, unlike in the earlier efforts, we have used unitarized amplitudes and hence our cross sections are naturally smaller than theirs. In Table VI, we show the results for the cross section and

 TABLE VII. As in Table VI with additional requirement of centrality ($|\eta^{\gamma, \text{jet}}| \leq 1.5$).

S.N.	$M_{q^*}^a$ (TeV)	$\Delta M_{\gamma-j}$ $\pm 3\Gamma(q^*)$ (GeV)	$\sigma(S+B)$ (pb)	$\sigma(B)$ (pb)	$\sigma(S^*)^b$ (pb)	Efficiency (S+B) (%)	Efficiency (B) (%)	Efficiency (S*) (%)
1	1.0	800–1200	4.75	2.14	2.61	0.668	0.304	36.22
2	1.5	1200–1800	0.87	0.41	0.45	0.123	0.059	30.64
3	2.0	1600–2400	2.27×10^{-1}	1.10×10^{-1}	1.16×10^{-1}	0.032	0.015	26.82
4	2.5	2000–3000	6.54×10^{-2}	3.43×10^{-2}	3.11×10^{-2}	0.009	0.004	28.66
5	3.0	2450–3550	2.21×10^{-2}	1.27×10^{-2}	9.40×10^{-3}	0.003	0.001	50.95
6	3.5	2900–4150	6.67×10^{-3}	3.20×10^{-3}	3.47×10^{-3}	0.165	0.079	20.55
7	4.0	3300–4700	2.64×10^{-3}	1.30×10^{-3}	1.34×10^{-3}	0.065	0.032	13.93
8	4.5	3700–5300	1.01×10^{-3}	4.59×10^{-4}	5.51×10^{-4}	0.025	0.011	9.92
9	5.0	4150–5850	3.99×10^{-4}	2.00×10^{-4}	1.98×10^{-4}	0.545	0.277	20.98
10	5.5	4500–6450	1.79×10^{-4}	9.78×10^{-5}	8.15×10^{-5}	0.246	0.135	13.78
11	6.0	5000–7000	6.51×10^{-5}	3.44×10^{-5}	3.07×10^{-5}	0.089	0.047	7.43

^aHere $f_1 = f_3 = 1.0$

^bPure new physics contribution evaluated by subtracting B from (S + B)

efficiency for S + B and B after all the kinematical and isolation selection cuts have been imposed for various M_{q^*} values. Table VII shows similar information for central events alone ($|\eta^{\gamma,\text{jet}}| \leq 1.5$).

XII. SYSTEMATIC UNCERTAINTIES

Since we have performed a detailed analysis including a realistic simulation of various detector effects and uncertainties for the CMS setup, here we present an estimation of systematic uncertainties. For this, we have considered only the dominant contribution both in the signal and the backgrounds. For both the signal and the γ + jet background we concentrate on the dominant process, viz. $qg \rightarrow q\gamma$. For the QCD dijet background, all the available processes in PYTHIA were used for the estimation of the uncertainty. We did not account for $q\bar{q} \rightarrow \gamma$ + jet, $W/Z(jj) + \gamma$, and $gg \rightarrow \gamma$ + jet as they contribute only a small fraction of the total background and systematic uncertainties in these can safely be neglected.

- (i) Choice of the parton distributions (PDF): To estimate the uncertainty in the cross sections due to the choice of the PDF, the former were recalculated for three additional PDFs, namely, CTEQ6L, CTEQ6M [51], and MRST2001 [52]. Using the LHApdf package [53], the results for each were compared to those for our default choice, namely, CTEQ5L [27]. While the resultant cross sections turned out to be higher for CTEQ6M (it should be noted that the CTEQ6M distributions are next-to-leading order (NLO) and hence their use with LO calculations is fraught with danger) and MRST2001 distributions, for CTEQ6L they turned out to be lower for almost all the signal points. As can be expected, the uncertainty in the cross section increases with M_{q^*} , simply because one starts to sample an ill-explored region in the (Q^2, x) plane. For CTEQ6M and MRST2001, the relative deviation varies between 2.3%–13.0% and 2.6%–14.2%, respectively, as M_{q^*} changes from 1 TeV to 6 TeV. For CTEQ6L, the variation was found to be within -4.5% to $+2.25\%$. These numbers are quite consistent with those applicable for the SM γ + jet process alone, for which the corresponding numbers are 5.6%–11.0% (CTEQ6M) and 6.0%–12.0% (MRST2001). Similarly, for the dijet background an uncertainty of 9%–16% (CTEQ6M) and 8.7%–16.5% (MRST2001) was estimated.

We have not only used different PDFs but have also evaluated uncertainty due to a given proton PDF by varying the errors on the parameters of the PDF fit itself. For this, we chose CTEQ6L (with NLO α_s and LO fit) and its 40 subset PDFs. The uncertainty was found to be $\sim \pm 1\%$ for a 1 TeV q^* state and -8.29% to $+10.93\%$ for a 5 TeV one. For QCD dijet and γ + jet backgrounds, these numbers were

found to be -9.81% to $+13.74\%$ and -8.04% to $+10.54\%$, respectively.

- (ii) Scale variation: To estimate the dependence of the signal and the background cross sections on the choice of the factorization scale Q (default value in our analysis being $\sqrt{\hat{s}}$), they were recalculated for three other values of the latter viz. $Q^2 = P_T^2$, $Q^2 = -\hat{t}$, and $Q^2 = 2\hat{s}$. The first two choices for the scale would have resulted in a higher cross section compared to $Q^2 = \hat{s}$ while the third one gives lower values. The deviation increases with M_{q^*} and ranges between 2.1%–11.3% for $Q^2 = -\hat{t}$, 10.6%–25.0% for $Q^2 = P_T^2$, and is in the $(-3.0\%, -5.0\%)$ range for the $Q^2 = 2\hat{s}$ case. For the QCD dijet background the maximum positive deviation was found to be $\sim 39\%$ while for γ + jet it was $\sim 26\%$. On the other hand with $Q^2 = 2\hat{s}$ these values are lower by $\sim 8\%$ and $\sim 5\%$, respectively, compared to $Q^2 = \hat{s}$. Thus, the overall significance of the signal remains largely unaltered.
- (iii) Higher-order effects: For the background, these have been studied in detail both theoretically and experimentally. For example, γ + jet production in the SM has been studied in depth using the NLO parton level Monte Carlo program JETPHOX [54,55]. Recently, a comparison of these predictions has been done with the Tevatron data [56]. Unfortunately, the P_T^γ -dependent shape of the triple differential cross section ($d^3\sigma/dp_T^\gamma dy^\gamma dy^{\text{jet}}$) for different pseudorapidity ranges is not explained satisfactorily by the NLO calculation. The reason is not hard to fathom. A comparison with data necessitates the imposition of isolation cuts. On the other hand, the NLO calculations depend crucially on the choice of isolation cuts and infrared safety needs to be taken care of. This has been discussed in Ref. [57]. Modulo such subtleties, an effective and easy way to incorporate higher-order effects is to include K factors. For γ + jet production, the K factor lies in the range 1.0–1.66 depending on the details of jet fragmentation (primarily, to a γ/π^0) [58]. While the K factor for our case is not known, in the large M_{q^*} limit it is not expected to be too different from the SM case. Close to threshold, the K factor is normally expected to be even bigger. However, given the attendant theoretical complications, we adopt a conservative approach and ignore all K factors in this analysis.
- (iv) Jet energy resolution: To incorporate finite detector resolutions, the photon and jet four momenta were smeared with energy resolutions as given in Sec. VI. For the photon P_T range considered in this analysis, we expect the constant term (C) to be the dominant source of error and it contributes about 0.55%. To estimate the effect of the jet energy resolution on this analysis, we redid this analysis smearing the four

momenta of the jet with an energy resolution of 100% for the barrel region and 150% for the endcaps and the forward regions. The effect was studied for two different mass states, viz. 1.0 TeV and 5.0 TeV. It was found that such a large worsening of the jet energy resolution would increase the luminosity required for a 5σ significance by about 30% (1%) for 1.0 TeV (5.0 TeV) mass states, respectively. However, if we increase the number of MC trials by a factor of 10 (to stabilize the peak value of LLR_{S+B}) then these numbers were found to be well within 2%.

It should be noted that the ATLAS detector at the LHC has a better jet energy resolution with the constant term being only $\sim 2\%$ [59] compared to $\sim 5\%$ in the CMS detector. On the other hand, the CMS ECAL has a better resolution than the ATLAS one owing to a smaller constant term. However, with the resolving power being dominated by the jet energy resolution, ATLAS should do somewhat better. In other words, our results correspond to a *conservative* choice.

- (v) Uncertainty due to preselection: The systematic uncertainty due to preselection in the P_T range of this study is found to be less than 1%.
- (vi) Luminosity error: For the CMS experiment, this error is expected to be $\sim 10\%$ for an integrated luminosity of 1 fb^{-1} [60] and $\sim 3\%$ for an integrated luminosity of 30 fb^{-1} [61].
- (vii) In Table VIII we show the dominant contributors to the total systematic uncertainty for two different mass points. The combined effect of all systematics on the required luminosity for discovery is also presented. Since the uncertainty in cross section due to choices of PDFs and scales (Q^2) are not independent, we varied them simultaneously. For this purpose, various combinations of scales ($2\hat{s}$, \hat{s} , $-\hat{t}$, P_T^2) and PDFs (MRST2001, CTEQ6M, CTEQ6L, CTEQ5L) are used. For estimating the uncertainty arising due to jet energy resolution

(JER) we increase the stochastic terms of JER to 100% in the barrel region and 150% in the endcaps, while the constant term (the dominant contributor for this analysis) is increased from 5% to 8% [62]. After smearing, the required integrated luminosity is reestimated. Since the uncertainty due to PDF choice, scale, and luminosity have a bearing on the cross section measurements, a linear addition (a more conservative choice compared to addition in quadrature) of these was applied on top of the uncertainty due to JER to evaluate the total combined effect. Our results show that systematic effects are indeed large and mainly dominated by scale and PDF uncertainties. We expect similar behavior for other mass states analyzed here.

XIII. CONCLUSIONS

To summarize, we have investigated the potential of using a direct photon (in association with a single hard jet) final state at the LHC to probe possible quark excitations. Such states arise naturally in a variety of scenarios, ranging from Kaluza-Klein excitations in extra-dimensional models to theories wherein the quarks themselves are composed of more fundamental objects (preons). And, as far as the concerns of the present analysis go, even other fundamental quarks (as often appear in theories with extended symmetries, gauged or global) could lead to similar signals and, hence, be discoverable.

In any such model, the “excited” states couple to their SM counterparts only through generalized (chromo)magnetic transition terms in an effective Lagrangian. This, then, allows for single q^* production (whether resonant or off shell) through quark-gluon fusion with the q^* then going into either two jets or to a quark and photon. Similarly, t -channel contributions exist too. Together, they lead to an alteration of the direct photon cross section with the quantum of deviation depending on both the mass M_{q^*} and the compositeness/excitation scale Λ . The deviation, apart from showing an invariant mass peak, is typi-

TABLE VIII. Major sources of systematic uncertainties for the signal and respective backgrounds and their effect on the required integrated luminosity for a 5σ discovery.

	Process	PDFs and scale uncertainties in cross section max. (min.) %	Luminosity error [60,61] ±%	Jet energy resolution (JER) effect on events in mass window ±%	$\int L \cdot dt$ without systematics [from Fig. 19(a)]	$\int L \cdot dt$ due to JER uncertainty only	$\int L \cdot dt$ with combined max. (min.) systematics
Signal M_{q^*}	2 TeV	19.71 (− 4.61)	10	−1.74	350 pb^{-1}	390 pb^{-1}	$336(430) \text{ pb}^{-1}$
Background	QCD dijet	58.08 (− 8.14)	10	0.55			
	γ + jet	19.76 (− 4.61)	10	0.99			
Signal M_{q^*}	5 TeV	35.91 (− 10.24)	3	−0.18	137 fb^{-1}	156 fb^{-1}	$126(171) \text{ fb}^{-1}$
Background	QCD dijet	51.32 (− 13.33)	3	0.37			
	γ + jet	37.45 (− 9.61)	3	0.18			

cally concentrated in the large p_T regime, especially for larger M_{q^*} and can be quite substantial.

Two points need to be noted here. The first and straightforward one relates to the width of the excited state. With $\Gamma(q^*)$ being typically quite large, a narrow-width approximation does not hold and the full matrix element needs to be incorporated. The second issue is more subtle and is connected to the nonrenormalizable nature of the effective Lagrangian. Since a naive use of a (chromo)magnetic dipole moment vertex leads to a cross section constant or even growing with the center of mass energy, the amplitude needs to be unitarized. This, understandably, leads to a suppression of the cross sections, a fact often ignored in experimental analyses, but included here.

Closely following the CMS experimental reconstruction algorithm for photon and jets, we devise a set of analysis cuts to extract the signal from the dominating backgrounds. This is limited not only to the mass peak, but also includes the distortion in the shape of the spectrum (this being particularly important for high q^* masses). We account for all major backgrounds to estimate the 5σ discovery limits in the mass range $M_{q^*}(= \Lambda)$ of 1–6 TeV.

With the imposition of moderate restrictions on the rapidities (as dictated by the detector acceptances), but

stringent cuts on the transverse momenta, the background can be beaten down severely without any damaging loss of signal. A most crucial ingredient is the application of reasonably stringent isolation criteria, as it helps control the orders of magnitude larger backgrounds from QCD dijet production with one jet faking a photon. The consequent exclusion limits that may be reached are very strong. While it may seem that these are still not as strong as some quoted in the literature [50], it should be realized that most of the latter have worked with a nonunitarized cross section and hence the two cannot be compared directly.

ACKNOWLEDGMENTS

B. C. C would like to thank S. Mrenna for discussions on $W\gamma$ production. S. B. and D. C. acknowledge support from the Department of Science and Technology (DST), India under Project No. SR/S2/RFHEP-05/2006. B. C. C acknowledges support from the DST, India under Project No. SP/S2/K-25/96-V. S. S. C would like to express gratitude to the Council of Scientific and Industrial Research, India for financial assistance and to Professor R. K. Shivpuri and Professor Raghuvir Singh for support and encouragement.

-
- [1] H. Harari and N. Seiberg, Phys. Lett. B **98**, 269 (1981); M. E. Peskin, in *Proceedings of the 1981 International Symposium on Lepton and Photon Interaction at High Energy, Bonn, Germany, 1981*, edited by W. Pfeil, p. 880; L. Lyons, Report No. OXFORD-NP-52-82, 1982; Prog. Part. Nucl. Phys. **10**, 227 (1983).
- [2] G. 't Hooft, in *Recent Developments in Gauge Theories*, G. 't Hooft *et al.* (Plenum, New York, 1980).
- [3] J. C. Pati, A. Salam, and J. A. Strathdee, Phys. Lett. B **59**, 265 (1975); H. Fritzsch and G. Mandelbaum, Phys. Lett. B **102**, 319 (1981); W. Buchmuller, R. D. Peccei, and T. Yanagida, Phys. Lett. B **124**, 67 (1983); Nucl. Phys. **B227**, 503 (1983); **B231**, 53 (1984); U. Baur and H. Fritzsch, Phys. Lett. B **134**, 105 (1984); X. Li and R. E. Marshak, Nucl. Phys. **B268**, 383 (1986); I. Bars, J. F. Gunion, and M. Kwan, Nucl. Phys. **B269**, 421 (1986); G. Domokos and S. Kovesi-Domokos, Phys. Lett. B **266**, 87 (1991); J. L. Rosner and D. E. Soper, Phys. Rev. D **45**, 3206 (1992); M. A. Luty and R. N. Mohapatra, Phys. Lett. B **396**, 161 (1997); K. Hagiwara, K. Hikasa, and M. Tanabashi, Phys. Rev. D **66**, 010001 (2002); Phys. Lett. B **592**, 1 (2004).
- [4] For a review and additional references, see R. R. Volkas and G. C. Joshi, Phys. Rep. **159**, 303 (1988).
- [5] K. Hagiwara, S. Komamiya, and D. Zeppenfeld, Z. Phys. C **29**, 115 (1985); U. Baur, M. Spira, and P. M. Zerwas, Phys. Rev. D **42**, 815 (1990); F. Boudjema, A. Djouadi, and J. L. Kneur, Z. Phys. C **57**, 425 (1993).
- [6] ALEPH Collaboration, Phys. Lett. B **385**, 445 (1996); ALEPH Collaboration, Phys. Lett. B **384**, 439 (1996); ALEPH Collaboration, Phys. Lett. B **250**, 172 (1990); ALEPH Collaboration, Phys. Lett. B **236**, 501 (1990); ALEPH Collaboration, Phys. Lett. B **236**, 511 (1990); DELPHI Collaboration, Phys. Lett. B **393**, 245 (1997); DELPHI Collaboration, Z. Phys. C **74**, 57 (1997); DELPHI Collaboration, Z. Phys. C **74**, 577 (1997); DELPHI Collaboration, Z. Phys. C **53**, 41 (1992); DELPHI Collaboration, Phys. Lett. B **274**, 230 (1992); DELPHI Collaboration, Phys. Lett. B **380**, 480 (1996); DELPHI Collaboration, Eur. Phys. J. C **8**, 41 (1999); L3 Collaboration, Phys. Lett. B **412**, 189 (1997); L3 Collaboration, Phys. Lett. B **401**, 139 (1997); L3 Collaboration, Phys. Lett. B **377**, 304 (1996); L3 Collaboration, Phys. Lett. B **370**, 211 (1996); L3 Collaboration, Phys. Lett. B **295**, 371 (1992); L3 Collaboration, Phys. Lett. B **251**, 321 (1990); L3 Collaboration, Phys. Lett. B **247**, 177 (1990); L3 Collaboration, Phys. Lett. B **250**, 205 (1990); L3 Collaboration, Phys. Lett. B **252**, 525 (1990); L3 Collaboration, Phys. Lett. B **502**, 37 (2001); OPAL Collaboration, Eur. Phys. J. C **1**, 45 (1998); OPAL Collaboration, Phys. Lett. B **393**, 217 (1997); OPAL Collaboration, Phys. Lett. B **391**, 197 (1997); OPAL Collaboration, Phys. Lett. B **386**, 463 (1996); OPAL Collaboration, Phys. Lett. B **385**, 433 (1996); OPAL Collaboration, Z. Phys. C **52**, 175 (1991); OPAL

- Collaboration, Phys. Lett. B **257**, 531 (1991); OPAL Collaboration, Phys. Lett. B **247**, 448 (1990); OPAL Collaboration, Phys. Lett. B **244**, 135 (1990); OPAL Collaboration, Phys. Lett. B **240**, 250 (1990).
- [7] I. Abt *et al.* (H1 Collaboration), Nucl. Phys. **B396**, 3 (1993); C. Adloff *et al.* (H1 Collaboration), Phys. Lett. B **525**, 9 (2002); **548**, 35 (2002); Eur. Phys. J. C **17**, 567 (2000); M. Derrick *et al.* (ZEUS Collaboration), Z. Phys. C **65**, 627 (1995); S. Chekanov *et al.* (ZEUS Collaboration), Phys. Lett. B **549**, 32 (2002).
- [8] R. Rückl, Phys. Lett. B **129**, 363 (1983); Nucl. Phys. **B234**, 91 (1984); W. Buchmuller, R. Rückl, and D. Wyler, Phys. Lett. B **191**, 442 (1987); P. Haberl, F. Schrempp, and H.U. Martyn, in *Physics at HERA, Hamburg, Germany, 1991*, edited by W. Buchmuller and G. Ingelman (DESY), p. 1133; W. Buchmuller and D. Wyler, Phys. Lett. B **407**, 147 (1997); N. G. Deshpande, B. Dutta, and X.-G. He, Phys. Lett. B **408**, 288 (1997).
- [9] D. Choudhury, S. Majhi, and V. Ravindran, J. High Energy Phys. 01 (2006) 027; S. Majhi, arXiv:0705.3071.
- [10] I. A. Bertram (D0 Collaboration), Report No. Fermilab-Conf-96/389-E, 1996.
- [11] F. Abe *et al.* (CDF Collaboration), Phys. Rev. Lett. **72**, 3004 (1994).
- [12] F. Abe, *et al.* (CDF Collaboration), Phys. Rev. Lett. **74**, 3538 (1995).
- [13] D0 Collaboration, D0 Note 5733-CONF, 2008.
- [14] CDF Collaboration, Report No. CDF/ANAL/JET/PUB/9609, 2008.
- [15] S. Ferrag (ATLAS and CMS Collaboration), J. Phys. Conf. Ser. **110**, 072010 (2008).
- [16] Ben Lillie, Jing Shu, and Tim M. P. Tait, J. High Energy Phys. 04 (2008) 087.
- [17] V. M. Abazov *et al.*, Phys. Lett. B **639**, 151 (2006).
- [18] B. Abbott *et al.*, Phys. Rev. Lett. **84**, 2786 (2000).
- [19] D. Acosta *et al.*, Phys. Rev. D **70**, 074008 (2004).
- [20] L. Apanasevich *et al.*, Phys. Rev. Lett. **81**, 2642 (1998).
- [21] N. Arkani-Hamed, *et al.*, Phys. Lett. B **429**, 263 (1998).
- [22] J. Weng *et al.*, CMS Note-2006/129, 2006.
- [23] B. Abbott *et al.* (D0 Collaboration), Phys. Rev. Lett. **86**, 1156 (2001); A. A. Affolder *et al.* (CDF Collaboration), Phys. Rev. D **64**, 092002 (2001).
- [24] P. Hasenfratz and J. Nager, Z. Phys. C **37**, 477 (1988).
- [25] S. Bhattacharya, S. S. Chauhan, B. C. Choudhary, and D. Choudhury, Phys. Rev. D **76**, 115017 (2007).
- [26] T. Sjostrand *et al.*, Comput. Phys. Commun. **135**, 238 (2001).
- [27] H. L. Lai *et al.* (CTEQ Collaboration), Eur. Phys. J. C **12**, 375 (2000).
- [28] CMS Collaboration, Report No. CERN/LHCC 2006-001 2006.
- [29] M. Pieri *et al.*, CMS Note-2006/112, 2006.
- [30] CMS Collaboration, Report No. CERN/LHCC 97-33.
- [31] G. C. Blazey *et al.*, arXiv:hep-ex/0005012 v2.
- [32] CMS TriDAS Project Data Acquisition and High-Level Trigger Technical Design Report No. CERN/LHCC 2002-26 CMS TDR 6.2.
- [33] S. V. Chenkov, arXiv:hep-ph/0211298.
- [34] S. Catani, Y. L. Dokshitzer, M. H. Seymour, B. R. Webber, Nucl. Phys. **B406**, 187 (1993).
- [35] J. M. Butterworth, J. P. Couchman, B. E. Cox, and B. M. Waugh, Comput. Phys. Commun. **153**, 85 (2003).
- [36] S. D. Ellis and D. E. Soper, Phys. Rev. D **48**, 3160 (1993).
- [37] G. Arnison *et al.*, Phys. Lett. B **132**, 213 (1983).
- [38] P. Schieferdcker *et al.*, CMS Analysis Note-2008/001, 2008.
- [39] CMS Collaboration, Report No. CERN/LHCC 97-31.
- [40] K. O. Mikaelian, M. A. Samuel, and D. Sahdev, Phys. Rev. Lett. **43**, 746 (1979).
- [41] M. A. Samuel and T. Abraha, arXiv:hep-ph/970633v1; U. Baur, S. Errede, and G. Landsberg, Phys. Rev. D **50**, 1917 (1994); V. M. Abazov *et al.*, Phys. Rev. Lett. **100**, 241805 (2008).
- [42] P. Gupta *et al.*, Eur. Phys. J. C **53**, 49-58 (2008).
- [43] L. Fano (CMS Collaboration), CMS Conference Report No. -2006/083, 2006.
- [44] J. Neyman and E. Pearson, Phil. Trans. R. Soc. A **231**, 289 (1933).
- [45] ALEPH Collaboration, DELPHI Collaboration, L3 Collaboration, OPAL Collaboration, and The LEP Working Group, for Higgs Boson Searches Phys. Lett. B **565**, 61 (2003).
- [46] M. G. Kendall and A. Stuart, *Inference and Relationships* (Hafner Publishing Company, New York, 1961), Vol. 2.
- [47] A. L. Read, J. Phys. G **28**, 2693 (2002).
- [48] F. James, CERN Program Library Long Writeup D506, 1998.
- [49] <http://root.cern.ch/drupal/content/users-guide>.
- [50] O. Cakir, R. Mehdiev, Phys. Rev. D **60**, 034004 (1999).
- [51] J. Pumplin, D. R. Stump, J. Huston, H. L. Lai, P. Nadolsky, and W. K. Tung, J. High Energy Phys. 07 (2002) 012.
- [52] A. D. Martin, R. G. Roberts, W. J. Stirling, and R. S. Thorne, Eur. Phys. J. C **23**, 73 (2002).
- [53] P. Bartalini, R. Cheirici, and A. De Roeck, CMS Note-2005/115, 2005.
- [54] PHOX programs, <http://lapweb.in2p3.fr/lapth/phox+family/main.html>.
- [55] P. Aurenche, M. Fontannaz, J. P. Guillet, E. Pilon, and M. Werlen, Phys. Rev. D **73**, 094007 (2006).
- [56] V. M. Abazov *et al.* (D0 Collaboration), arXiv:0804.1107v2.
- [57] S. Catani, M. Fontannaz, J. P. Guillet, and E. Pilon, J. High Energy Phys. 05 (2002) 028.
- [58] Z. Bern, L. Dixon, C. Schmidt, Phys. Rev. D **66**, 074018 (2002).
- [59] ATLAS Collaboration, Report No. CERN/LHCC 99-14.
- [60] CMS Collaboration, J. Phys. G **34**, 995 (2007).
- [61] S. Abulin *et al.*, CMS Note-2006/122, 2006.
- [62] Thesis by Efe Yazgan [CERN Report No. CERN-THESIS 2007-052, 2007].